Geological Quarterly, 2025, 69, 3
DOI: http://dx.doi.org/10.7306/gq.1776

Mineralogy, geochemistry and genesis of clays in the Tekneli and Delikkaya (Turkey) carbonate-hosted sulphide and non-sulphide Pb-Zn deposits

Hülya ERKOYUN[1, *] and Ali JAWADI[1]

[1] Eskişehir Osmangazi University, Department of Geological Engineering, TR-26040 Eskişehir, Turkey; ORCID: 0000-0001-2345-6789 [H.E.], 0000-0001-2345-6785 [A.J.]

Erkoyun, H., Jawadi, A., 2025. Mineralogy, geochemistry and genesis of clays in the Tekneli and Delikkaya (Turkey) carbonate-hosted sulphide and non-sulphide Pb-Zn deposits. Geological Quarterly, 69, 3; https://doi.org/10.7306/gq.1776

Associate editor: Stanisław Mikulski

The Tekneli and Delikkaya carbonate-hosted sulphide and non-sulphide Pb-Zn deposits formed along faults and karstic cavities under the control of hydrothermal fluids with subsequent supergene oxidation in limestones and dolomitic limestones. Sulphide (galena, sphalerite, pyrite) and non-sulphide minerals (smithsonite, cerrusite, goethite, and hematite) were found to be present. XRD patterns and Fourier Transform Infrared (FTIR) spectroscopic analyses show that fraipontite is predominant among Zn clay minerals, with lesser amounts of sauconite (Zn smectite), and illite. SEM images of smectite, illite, chlorite from karst-filled "red clays" coating and filling pores suggest their detrital origin. Zn clays (fraipontite and sauconite) developed *in situ* on detrital illite and mixtures of detrital red clays. SEM-EDX analyses show that the fraipontite contains a higher content of Zn (14.8%) compared to sauconite (10.2%). The plots of Al_2O_3 vs. SiO_2, TiO_2 vs. Al_2O_3, light rare earth element (LREE) enrichment, nearly flat heavy rare earth element (HREE) patterns, and Eu and Ce anomalies in the clays, suggest sediments dominated by felsic and some mafic rock sources and derived from seawater or porewater under oxidizing conditions. The enrichment relative to upper crustal compositions (UCC) indicates alteration of feldspar under warm and humid climate conditions during weathering. The red clay type residual clays originated from ophiolitic, carbonate, mudstone, siltstone, and marl host rocks and were transported to karst cavities as breccia matrices by groundwater after limestone dissolution in the study area. Zn clays related to red residual clays in the karstic cavities formed either by direct precipitation of meteoric fluids or grew over detrital illite.

Key words: Niğde, Kayseri, Pb-Zn deposit, alteration, mineralogy, geochemistry.

INTRODUCTION

The carbonate-hosted Missisippi Valley Type deposits include sulphide and abundant non-sulphide ores. Non-sulphide ores comprise Zn carbonates (such as smithsonite, hydrozincite), Zn-silicates (such as willemite, hemimorphite), Zn-oxides (such as zincite, franklinite), Zn-rich clays (such as sauconite, fraipontite) associated with Pb-carbonates (such as cerussite), Pb-sulfates (such as anglesite), Fe-carbonate (such as siderite), and Fe- (hydr)oxides (such as goethite, hematite) (Boni and Large, 2003; Coppola et al., 2008).

Non-sulphide deposits have been classified as supergene and hypogene, based on mineralogical and geological characteristics and genetic setting (Large, 2001; Hitzman et al., 2003). The supergene type formed by oxidation of metal sulphides and weathering (Pirajno et al., 2010) and may be subdivided into direct-replacement, wall-rock replacement, and karst-fill deposits (Hitzman et al., 2003). Since the 21th century, the development of new technologies (solvent-extraction and electro-winning processes, the Wälz modernization), non-sulphide Zn (and Pb) deposits are growing in economic importance (Large, 2001; Boni and Large, 2003; Hitzman et al., 2003). The non-sulphide deposits compared to sulphide deposits have high metal contents, extract is easier and faster, have a scarcity or absence of Pb, S and other undesirable elements, and enable low-energy recycling (Boni, 2003; Reich and Vasconcelos, 2015). The tonnage of these deposits is between 1–200 Mt and their grade is between 7–30% Zn (Reynolds et al., 2003) and examples of deposits of this size in the world include Skorpion (Namibia), Mae Sod (Thailand), Lan Ping (China), Angouran and Mehdi Abad (Iran), Shaimerden (Kazakhstan), Jabali (Yemen), Sierra Mojada (Mexico), and Franklin/Sterling Hill (USA) (Boni, 2003).

Zn-clays (fraipontite, sauconite) have been described in many supergene zinc deposits because of their high sorption capacities for zinc (Churakov and Dähn, 2012), and their economic importance has increased with recent extraction methods. Fraipontite is a Zn-containing clay in the kaolinite-serpentine group found in supergene zinc deposits in Belgium (Fransolet and Bourguignon, 1975), Iberia (Calvo et al., 2007; Will et al., 2014), Italy (Merlino and Orlandi, 2001), and Kazakhstan (Chukhrov, 1956). Sauconite is a trioctahedral

* Corresponding author, e-mail: hlerkoyun08@gmail.com

Received: December 19, 2023; accepted: February 12, 2025; first published online: April 7, 2025

saponite-like Zn-bearing smectite common in non-sulphide deposits in Northern America (Ross, 1946), Peru (Boni et al., 2009; Mondillo et al., 2014, 2015), South Africa (Kärner, 2006; Terracciano, 2008; Boni et al., 2011), and Iran (Daliran et al., 2007). Zn- clays are usually mixed residual clay minerals similar to those in the reported Bou Arhous non-sulphide deposit in the Moroccan High Atlas (Buatier et al., 2016).

Residual red clay minerals (kaolinite, illite, smectite) formed in weathering conditions after Jurassic limestone dissolution in the Bou Arhous Zn-Pb ore deposit of Morocco (Choulet et al., 2016), and montmorillonite in the Midwest Taurides, Bolkarlar, Aladağlar-west Zamantý and East Zamantý regions in Turkey (Özbek, 2014). Halloysite and kaolinite occur in the Paleozoic limestones of a Belgian non-sulphide Pb-Zn deposit formed under the supergene weathering conditions (Coppola et al., 2008). These clays were precipated in karstic cavities with massive alteration, as in carbonate-hosted Dongmozhazhua Pb-Zn deposit associated with Permian-Triassic limestones in South Qinghai, China (Liu et al., 2011).

The carbonate-hosted Pb-Zn deposits of the Eastern and Central Taurides consist of widespread Zn mineralization that contains mixed sulphide and mainly non-sulphide ores (Hanilçi et al., 2019). The Tekneli (Çamardı-Niğde) and Delikkaya (Yahyalı-Kayseri) carbonate-hosted Pb-Zn deposits (MVT) are the most important underground operated mines in the Eastern Tauride Mountains. The Tekneli and Delikkaya Pb-Zn deposits have a reserve (30% sulphide and 70% non-sulphide ore) of up to 2.751.800 tons at average grades of 27.50% Zn, and 2.86% Pb (Mengeloğlu, 1998; Hanilçi, 2003; Pekdemir, 2010) and 2,500,000 tons at average grades of 35–40% Zn, and 5.0–6.0% Pb, respectively (Hanilçi and Öztürk, 2011). In the Tekneli deposit, Zn is produced mostly from smithsonite, zincite and hydrozincite with a small amount of sphalerite, while in the Delikkaya deposit, mostly Zn is produced from smithsonite, zincite, hydrozincite while Pb is produced in small amounts from galena and cerussite. Mining activities in the region began in the Bronze Age by the Hittites and continued from the Byzantine, Seljuk and Ottoman periods until today (Yıldırım, 2008).

In the past there have been different proposals to explain the Pb-Zn ores in the Aladağ region (e.g., hydrothermal activity related to magmatism; Temur, 1992; Altuncu, 2000; Kuşcu and Cengiz, 2001; Yalçın and Altuncu, 2004; Şahin, 2005; Çiftçi et al., 2006), but nowadays the consensus is they have features of typical MVT deposits, with no contacts with igneous rocks, and they occur in platform carbonates (limestones and dolostones) (Öztürk and Hanilçi, 2009; Hanilçi and Öztürk, 2011; Kahya, 2018).

The geology, mineralogy, petrography, geochemistry, isotopic features (S isotopes) and genesis of the Pb-Zn deposits of the Bolkardağý and Aladağlar regions in the Central and Eastern Taurides were studied by Demir and Bingöl (2000), Ceyhan (2003), Yalçın and Altuncu (2004), Pekdemir (2010), Özbek (2014), Tümüklü et al. (2018) and Kahya, (2018). Clays in the Pb-Zn deposits in the central and eastern Taurides have not been studied in detail and have often been neglected (Özbek, 2014). This study examines the formation of residual and Zn-bearing clays and associated ore minerals based on detailed mineralogical, micromorphological, geochemical and stable isotope analyses, to describe the genesis of clays in the sulphide and non-sulphide Tekneli and Delikkaya Pb-Zn deposits, which have no recent history of study.

GEOLOGICAL SETTING

The study area is situated in the Upper Devonian–Upper Cretaceous Aladağlar Unit which has a nappe structure and consists of shelf-type carbonate and siliciclastic rocks in the Eastern Tauride region (Demirören, 2010). The tectonostratigraphy of the nappe slices from bottom to top are represented as the Yahyalı, Siyah Aladağ, Çataloturan, Mineratepeler and Beyaz Aladağ nappes, the Aladağ Ophiolite Melange and the Aladağ Ophiolite Nappe (Fig. 1; Ayhan, 1983; Tekeli et al., 1983). The Siyah Aladağ Nappe consists of upper Devonian siltstone, quartzite, and reef limestone occurring in Aladağlar-Zamantı region (Fig. 2; Tekin, 2009). These units are overlain conformably by a Carboniferous quartzite-limestone alternation (Çelik et al., 2007; Tekin, 2009). The Lower Permian is characterised as a limestone with *Girvanella* guide-levels, locally with dolomitic limestone levels (Çelik et al., 2007). The Tekneli deposit developed in Upper Permian strata comprising an algae-rich assemblage (named the *Mizzia* limestone) containing quartzite intercalations and overlain conformably by Triassic units (Hanilçi and Öztürk, 2011; Kuşcu and Cengiz, 2001). The Triassic units consist of oolitic limestone and mudstone-marl-siltstone (Çelik et al., 2007). The Delikkaya deposit occurs within Jurassic laminated and thin-bedded clayey limestone, massive limestone, bituminous/clayey limestone and dolomitic limestone units (Hanilçi and Öztürk, 2005, 2011). The ophiolite occurs between the Siyah Aladağ units and a Jurassic–Cretaceous nappe in the study area.

The study area was affected by a NE–SW trending strike-slip (Ecemiş) fault, and N–S, E–W and NE–SW-trending reverse, normal and oblique faults (such as Göktepe fault; Dilek and Whitney, 2000; Şahin, 2005; Çelik et al., 2007), and the Tekneli anticlinorium and folds (Pekdemir, 2010). During secondary folding, faults formed during the primary folding process were reactivated (Çelik et al., 2007).

DESCRIPTION OF THE TEKNELI AND DELIKKAYA PB-ZN DEPOSITS

The Tekneli and Delikkaya Pb-Zn deposits have an irregular geometry formed by karstification. Both the Tekneli and Delikkaya Pb-Zn deposits have a vein and karstic cavity-filling type geometry controlled by the fault zone and are discordant to the limestone/dolomitic limestone. Red clay materials, clastic fragments of ore and limestone, detrital quartz, smithsonite and goethite filled these cavities. The clays, silty clays, mudstone and limestone, and the gossan, smithsonite, galena+sphalerite ore were analysed in samples obtained from the underground ore deposits and stocks.

TEKNELI PB-ZN DEPOSIT

The Tekneli Pb-Zn deposit is located in a 2–3 km zone that extends N-S along the axis of the Tekneli anticlinorium and consists of a mixed sulphide-non-sulphide ore body (Fig. 1; Tekin, 2009; Pekdemir, 2010). There are two parallel veins on the east limb of the anticlinorium and one on the west limb (Eren et al., 1993; Demir, 1998). The longest, No. 1, vein is 2.2 km long and 1–8 m thick (Demir, 1998). The sulphide ores mainly include sphalerite, minor galena, pyrite, arsenopyrite and chalcopyrite, while non-sulphide ores consist of abundant smithsonite, rare hydrozincite, zincite, and cerrusite associated with abundant goethite and hematite (Çopuroğlu, 1996; Demir, 1998; Tekin, 2009). The karst-fill type ore deposited within the limestones developed in a limited way due to the low porosity of the limestone, being mostly oxidised and converted into Zn-Pb oxide-carbonate minerals (Demir, 1998).

The deposit occurs within limestone and dolomitic limestone of Permian age which is dark grey, hard, massive with layers 30–70 cm thick, bearing mesh-form silica and calcites (Fig. 3C). The clays are brown and reddish, plastic, blocky, stained and developed as karst-fills (2–5 cm wide), called red clays, at the contact with limestones and intercalated with gossan unit and ore (1–1.5 m thick; Fig. 3A, B). These clays contain

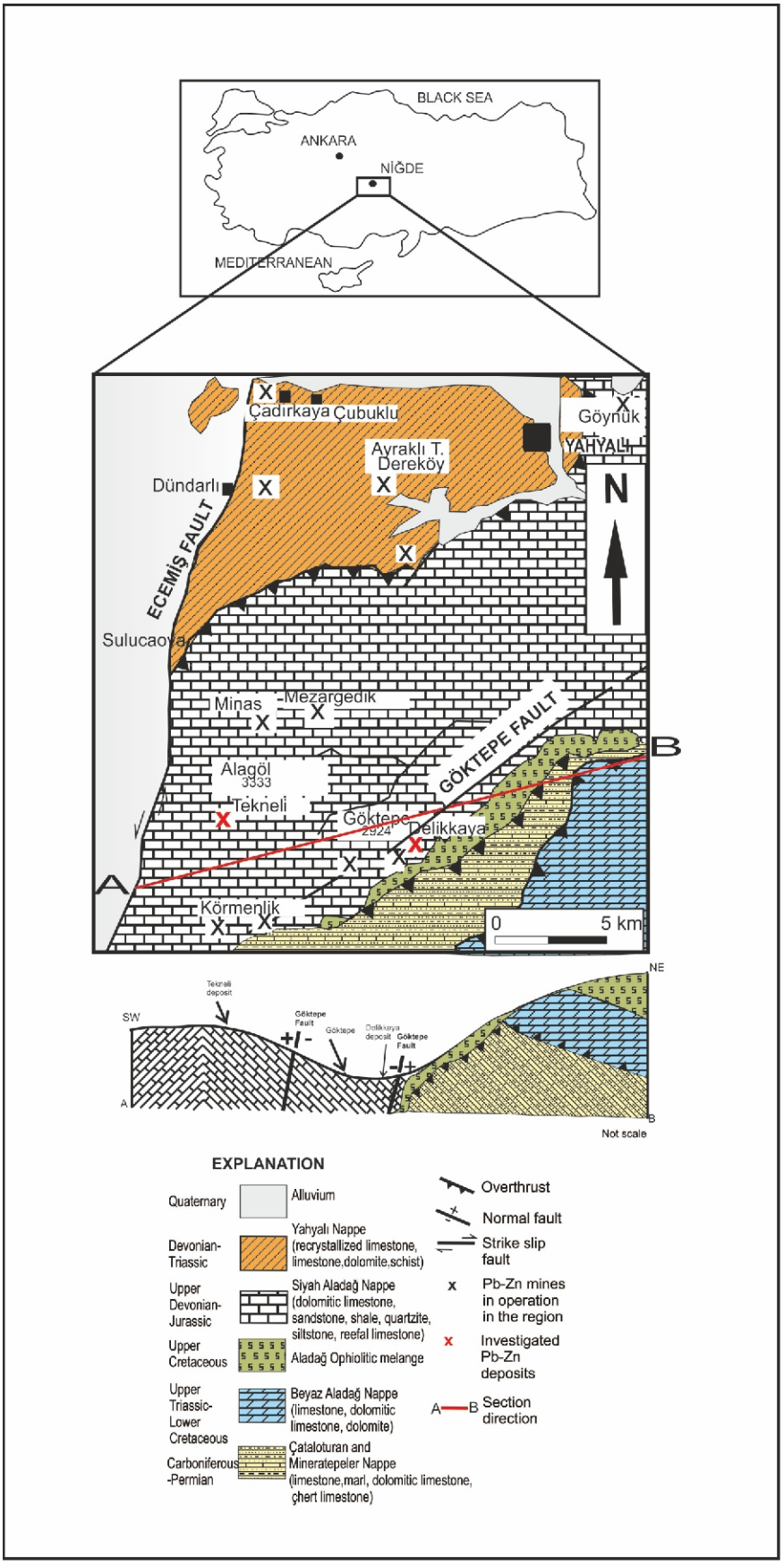

Fig. 1A – geological maps of the Tekneli (Niğde) and Delikkaya Pb-Zn deposits (Tekeli et al., 1983) and locations of the carbonate-hosted Pb-Zn deposits (modified after Hanilçi and Öztürk, 2011); B – geological cross-section through the study area

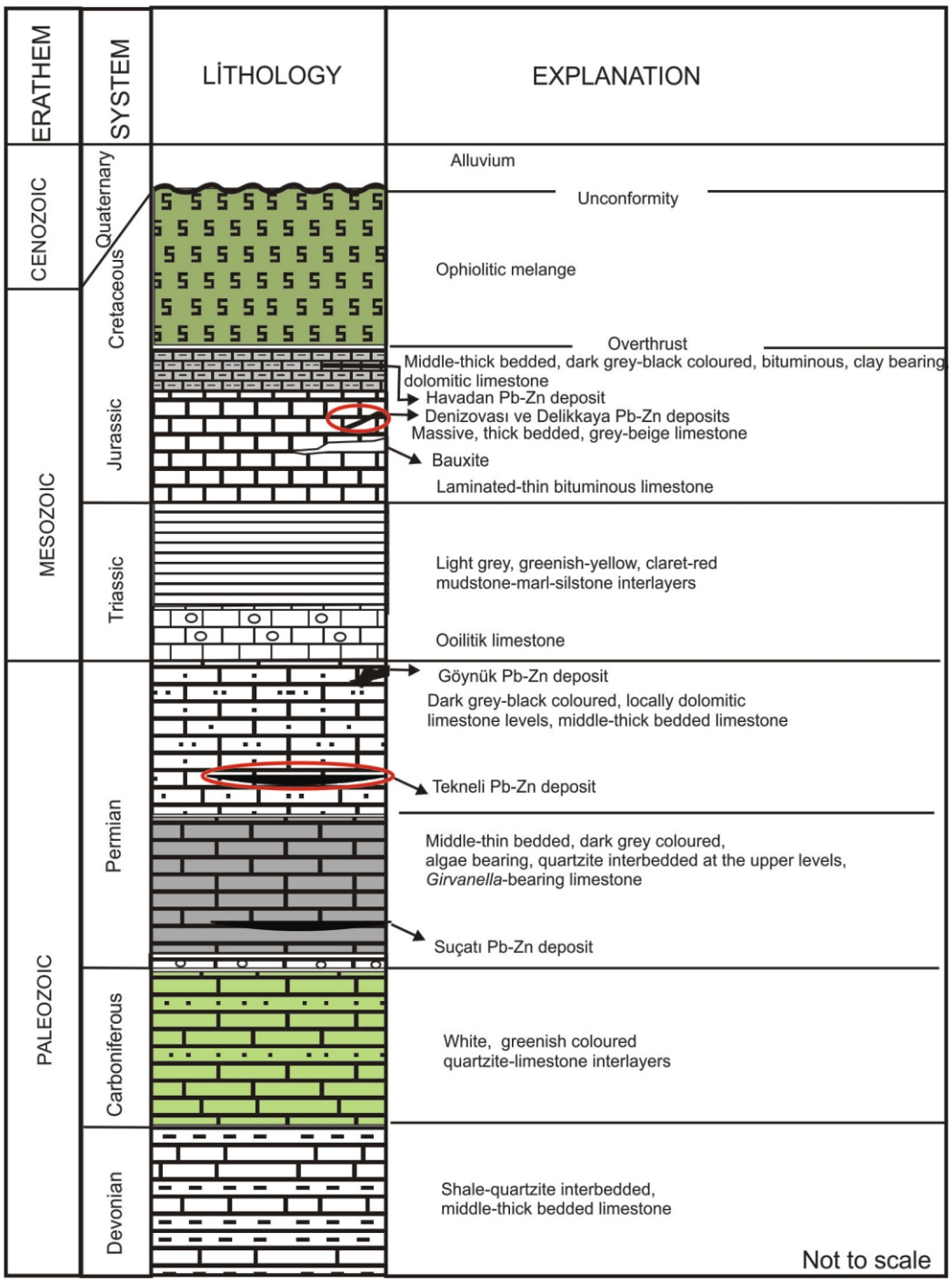

Fig. 2. Stratigraphic section of the Siyah Aladağ Nappe (Hanilçi, 2003)

ore mineral grains. The limestone is conformably overlain by siltstone which is brown, and laminated to thin-bedded (with beds 10–40 cm thick). The sulphide ore (sphalerite and galena) is grey, Fe-oxide-stained and occurs as vein-fills along fault zones and karst-fills. The non-sulphide ore (smithsonite) is white, grey and brown and has colloform texture in karstic cavities of carbonate rocks. Gossan representing the oxidation of Fe, Zn and Pb sulphides is hard, compact, yellow and red-brown, filling karstic cavities at the top. These unit contains 0.5 cm-diameter black galena and sphalerite nodules (Fig. 3D, E).

DELIKKAYA PB-ZN DEPOSIT

The Delikkaya deposit is located 12 km NE of Tekneli and the ore has a vein and karst-infill structure controlled by faults (Demirören, 2010). The skeleton and breccia sulphide ore indicate that the karstification and tectonic processes post-dated the formation of the ore (Hanilçi and Öztürk, 2011). The deposit contains both sulphide and carbonate-oxide ore zones, with three zones recognised based on the chemistry, from top to bottom: (a) iron cap zone (gossan and clays); (b) a middle Pb- and Zn-rich zone; (c) a zinc carbonate zone (Hanilçi et al.,

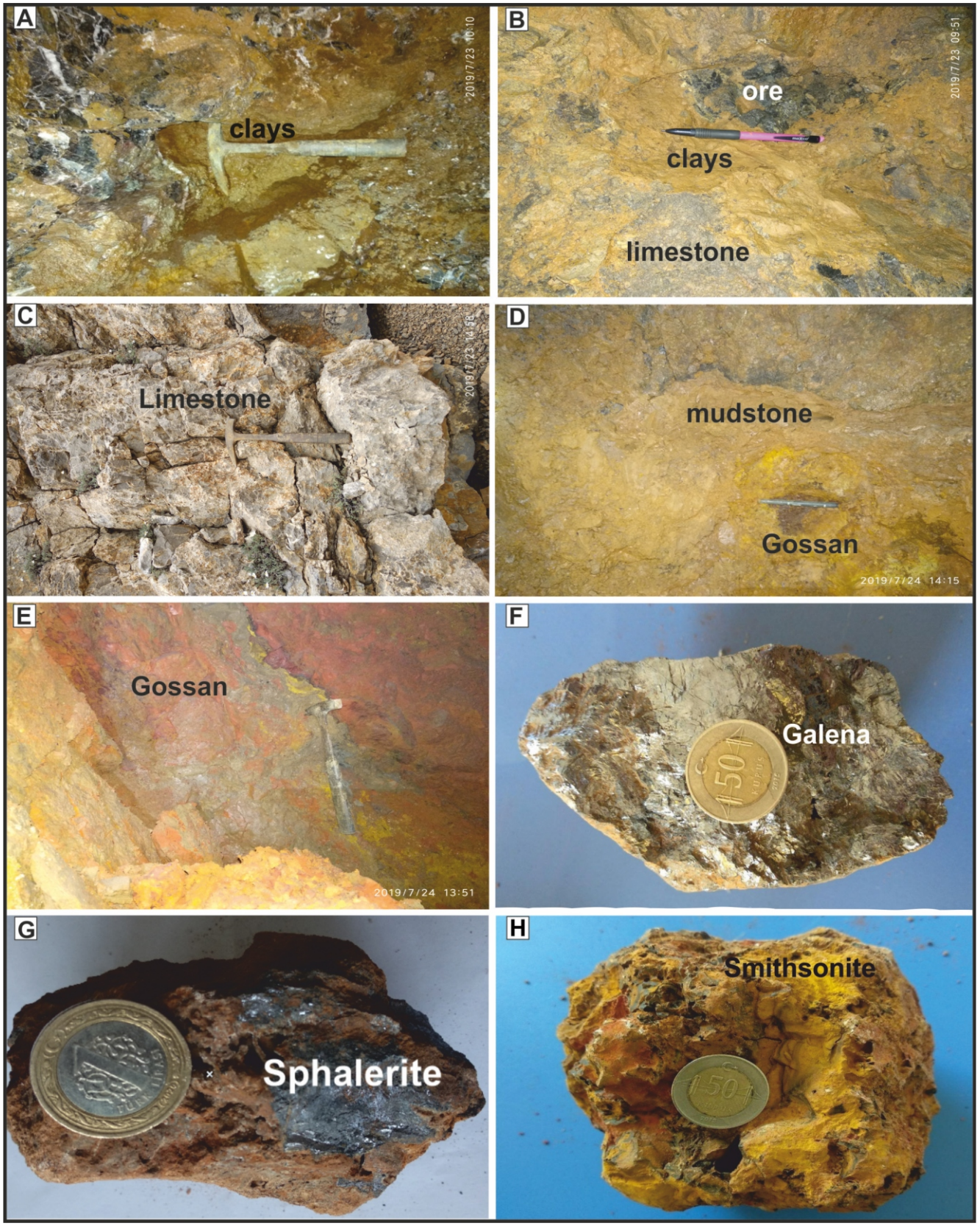

Fig. 3. Field photographs of Tekneli and Delikkaya Pb-Zn deposits

A, **B** – clay is developed generally at the contact with limestone and filling cracks; **C** – limestone sample collected underground; **D** – yellowish-brown to reddish-brown gossan unit associated with mudstone; **E** – reddish-brown gossan unit; **F** – galena taken from the production stock; **G** – sphalerite taken from the production stock; **H** – smithsonite taken from the production stock

2019). The ore zone is ~50 m in length and 130 m deep and is discordant to the wall rock (Hanilçi et al.,2019). The karstic cavities range between 20–30 m in width and 50–60 m in length (Hanilçi, 2003).

Sulphide ores of the Delikkaya deposit comprise abundant galena and sphalerite, rare pyrite, marcasite and chalcopyrite, while non-sulphide ores consist of abundant smithsonite, rare cerrusite, anglesite, hydrozincite, zincite and siderite associated with abundant goethite and hematite (Hanilçi and Öztürk, 2011).

The deposit occurs within a clayey limestone and dolomitic limestone of Jurassic age and is light to dark grey, hard, massive, thick-bedded (10 cm to 2 m), with calcite veinlets, and a clay cover (Fig. 3C). The clays are brown, plastic, blocky, with Fe-oxide stains and developed by filling karst (2–5 cm width) at the contact of the limestones and intercalated with gossan unit and ore (0.7–1.2 m thick). The associated brown siltstone and mudstone succession which relate to the red clays is laminated to thinly bedded (max. 13.5 cm thick), lenticular, with a mixture of silt- and clay-sized particles and a plastic character (Fig. 3D). Galena ore is observed as a grey brecciated zone within the limestone, its outer parts white-yellow and oxidised (cerussite+anglesite; Fig. 3F, G). The smithsonite is yellowish-brown with a colloform texture in karstic caves. Gossan representing the oxidation of Fe, Zn and Pb sulphides is hard, compact, yellow and red-brown, filling karstic cavities at the top (Fig. 3H).

MATERIALS AND METHODS

Forty two representative lithological samples were collected from underground, underground production stock and old surface mines of the Tekneli and Delikkaya deposits

Limestone samples were examined under a polarizing microscope (*Nikon-LV 100Pol*). The ore (galena and sphalerite) and gossan samples were studied under a polished-section microscope (*Leitz MPV-SP*). X-ray powder diffractometry (XRD) analysis was carried out using a *Rigaku D/Max-2200*, Ultima PC instrument. The XRD analyses were performed using CuK radiation with a scanning speed of °2 per minute. Randomly oriented mounts of powdered whole-rock samples were scanned to determine the mineralogy of each bulk sample. Samples for clay fractions were separated using sedimentation after 24 h dispersion in distilled water and centrifuging the suspension for 10 min at 4000 rpm using a *Hettich 32A* centrifuge. Oriented specimens of the <2 μm clay fractions were prepared from each sample, air-dried, ethylene glycol solvated, and heated at 550°C for 2h to determine the mineralogy of the clay minerals. Semi-quantitative abundances of the rock-forming minerals were obtained using Brindley's (1980) external standard method. The relative abundances of clay-mineral fractions were determined using their basal reflections and the mineral intensity factors of Moore and Reynolds (1989).

Scanning electron microscopy (SEM) studies were performed at the Eskişehir Osmangazi University (Turkey) using a *JEOL JSM 84A* instrument equipped with an energy dispersive X-ray (EDX) detector. The surface of each sample was mounted onto an aluminum sample holder with double-sided tape and thin gold coating (350 Å) using a Giko ion coater.

Fourier transform infrared (FTIR) spectroscopic analysis was performed on pressed pellets of powdered one-clay sample (<2μm) mixed with KBr at 4 cm^{-1} resolution, in the 4000–400 cm^{-1} range, using a PerkinElmer Spectrum Two spectrometer at Eskişehir Osmangazi University ARUM, Türkiye.

Chemical analyses of 17 dolomitic limestone, limestone, gossan and clay samples were performed at the Bureau Veritas Mineral Laboratories (Vancouver, Canada) using inductively coupled plasma–atomic emission spectroscopy (ICP-AES) for major and trace elements and inductively coupled plasma–mass spectrometry (ICP-MS) for rare earth elements (REE) and determined from an aqua-regia digestion. Loss on ignition (LOI) values were determined from the mass differences before and after ignition at 1000°C. Total organic carbon (TOC) values were determined by ignition followed by measurement by an infrared spectrometric cell in a LECO Carbon Analyzer (LECO Corporation, Saint Joseph, Michigan, USA) by Bureau Veritas, Vancouver, Canada.

The rare earth elements comprised the lanthanide elements (La-Lu), Y per IUPAC (2005). The measured concentrations of the REE were normalized relative to upper continental crust (UCC; Taylor and McLennan, 1985) to better show the relative changes in REE concentrations due to crustal processes such as weathering and diagenesis (Rudnick and Gao, 2014).

RESULTS

PETROGRAPHIC DESCRIPTION

The mineralized limestone-dolomitic limestone samples are characterized by micritic, microsparitic, and sparitic (0.05–0.1 mm) calcite, partially argillized and sericitized orthoclase, subrounded and monomineralic quartz, biotite, muscovite, and euhedral dolomite (Fig. 4A–D). Partially or completely opacitized biotite and opaque minerals are also present (Fig. 4C). Argillized muscovite occurs as a minor component (Fig. 4D). Brown-black argillized and Fe-(oxyhydr)oxidizied phases developed as stains and infill fracture-cracks of the samples (Fig. 4C, E, F). Rounded and ellipsoidal forms of pellets w0.1–0.9 mm in diameter are filled with micritic and microsparitic calcite. Foraminifera were observed in the Fe-oxidized micritic groundmass (Fig. 4G). The algae occur as rounded forms and thin, long branches and are filled with calcite (Fig. 4H). Hyaline and porcellanous shell fragments were also determined in the carbonate units.

XRD DETERMINATIONS

Fraipontite is an abundant alteration product in the Tekneli and Delikkaya deposits, accompanied by illite/mica, sauconite, smectite and chlorite and non-clay minerals such as quartz, calcite, dolomite, feldspar, amphibole, pyrite, cerussite, smithsonite, goethite and hematite (Table 1 and Fig. 5). Silica alteration (detrital quartz and silicification) was determined in the clays and the gossan units. Argillization occurs along the fractures and cracks around the ore in the form of red clays such as illite and smectite associated with pyrite, hematite, goethite and quartz. The mudstone consists of smectite, kaolinite, chlorite, quartz, accessory mica and calcite. The siltstone is composed of calcite, dolomite, accessory mica, kaolinite, quartz and feldspar. Fe-(oxyhydr)oxidation to give goethite and a small amount of hematite is observed. Pyrite occurs in both the gossan zone and the clays. The presence of chlorite was also determined in the gossan.

Well-ordered fraipontite was identified by (001), (002) and (003) reflections at 7.1, 3.57, and 2.38 Å, respectively (Fig. 5; Buatier et al., 2016). The 061 reflection (at 1.50 and 1.54 Å) indicate that Zn is the major cation in the octahedral position of the fraipontite (Kloprogge et al., 2001; Choulet et al., 2016) of

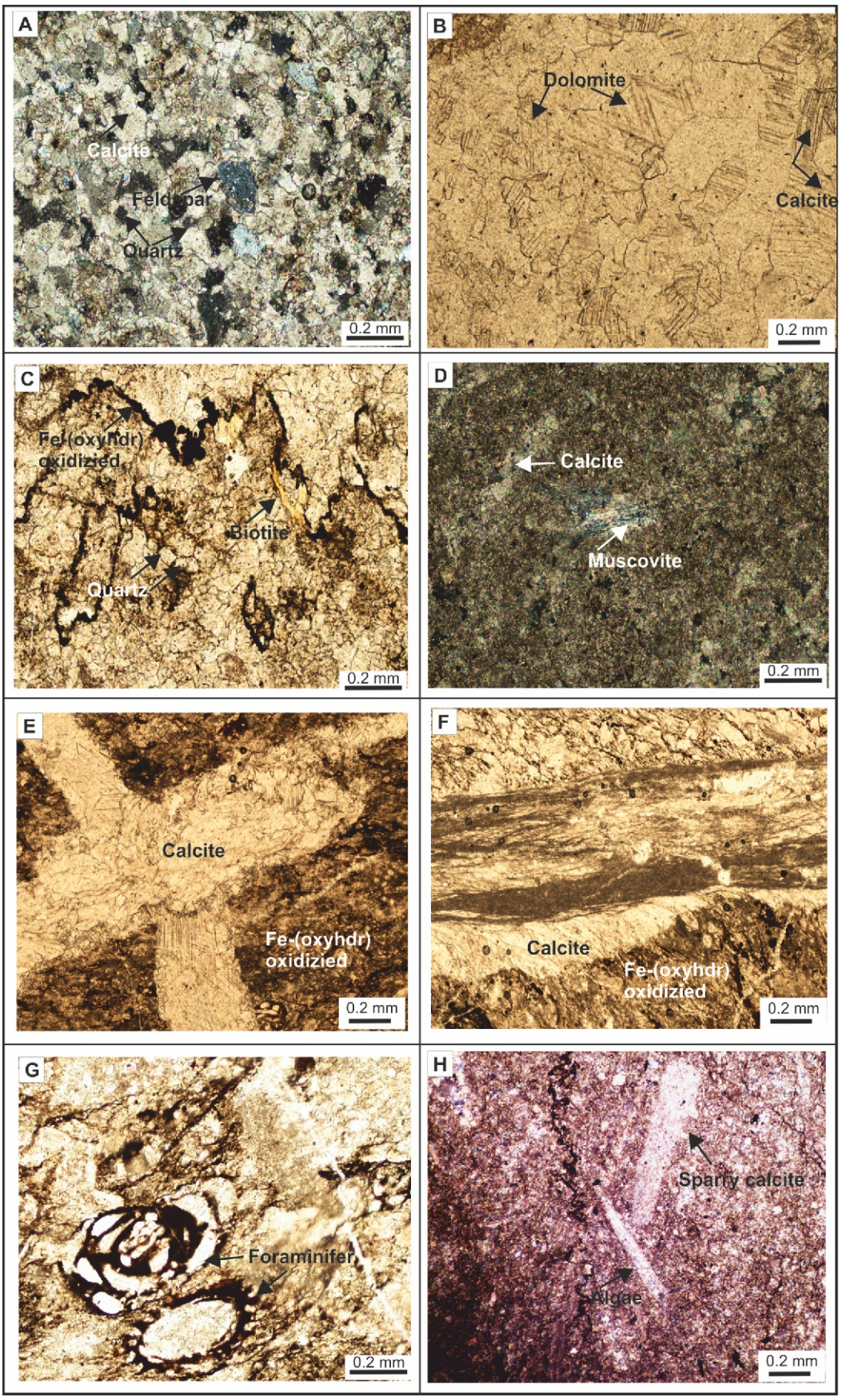

Fig. 4. Photomicrographs of the Tekneli and Delikkaya limestone-dolomitic limestone

A – argillized and sericitized feldspar, quartz and calcite minerals, cross-polarised light (TN-5); **B** – euhedral dolomite with calcite fragments, plane polarised light; **C** – biotite and Fe-(oxyhdr) oxidized, plane polarised light (TN-5); **D** – argillized muscovite and calcite, cross-polarised light (TN-8); **E** – calcite veins in fracture-crack fillings and Fe-(oxyhdr) oxidized, plain polarised light (TN-14); **F** –calcite infill in fracture-crack, plain polarised light (TN-14); **G** – foraminifera in iron oxidized micritic groundmass, plain polarised light (TN-14); **H** – algae filled with calcite, plain polarised light (TN-8)

Table 1

Mineral composition of samples from the Tekneli and Delikkaya Pb-Zn deposit

Sample	Litology	Sme	Sau	Ilt/ Mca	Frp	Kao	Chl	Qz	Fsp	Smith	Cal	Dol	Amp	Cer	Hem	Py	Gth
Tekneli Deposit																	
TN-13	Gossan			acc	+		acc	+++	acc							+	
TN-16	Clays			acc	++		acc	+								++	
TN-17	Clays	acc		acc	+			+++			+					acc	
TN-19	Siltstone			acc		acc		acc	acc		+++	++				acc	
TN-20	Clays	acc		++	++			+	acc								
TN-21	Clays	acc		acc	+			+++	acc		+		acc				
Delikkaya Deposit																	
DL-3	Clays	acc		acc	+			++++							acc		
DL-4	Mudstone	++		acc		+	+	++			acc						
DL-5	Gossan	+	acc	acc	+		acc	++									+
DL-6	Clays	acc		+	+			+++	acc					acc			
DL-8	Cerussite ore								acc					+++++			acc
DL-10	Cerussite ore													+++++			
DL-11	Clays	acc		acc	++			+++									
DL-14	Gossan																+++++
DL-15	Simithsonite ore									+++++	acc						

Sme – smectite, Sau – sauconite, Ilt/Mca – illite/mica, Frp – fraipontite, Kao – kaolinite, Chl – chlorite, Qz – quartz, Fsp – feldspar, Smith – smithsonite, Cal – calcite, Dol – dolomite, Amp – amphibole, Cer – cerrusite, Hem – hematite, Py – pyrite, Gth – goethite, acc – accessory, + – relative abundance of mineral (mineral name abbreviations after Whitney and Evans, 2010)

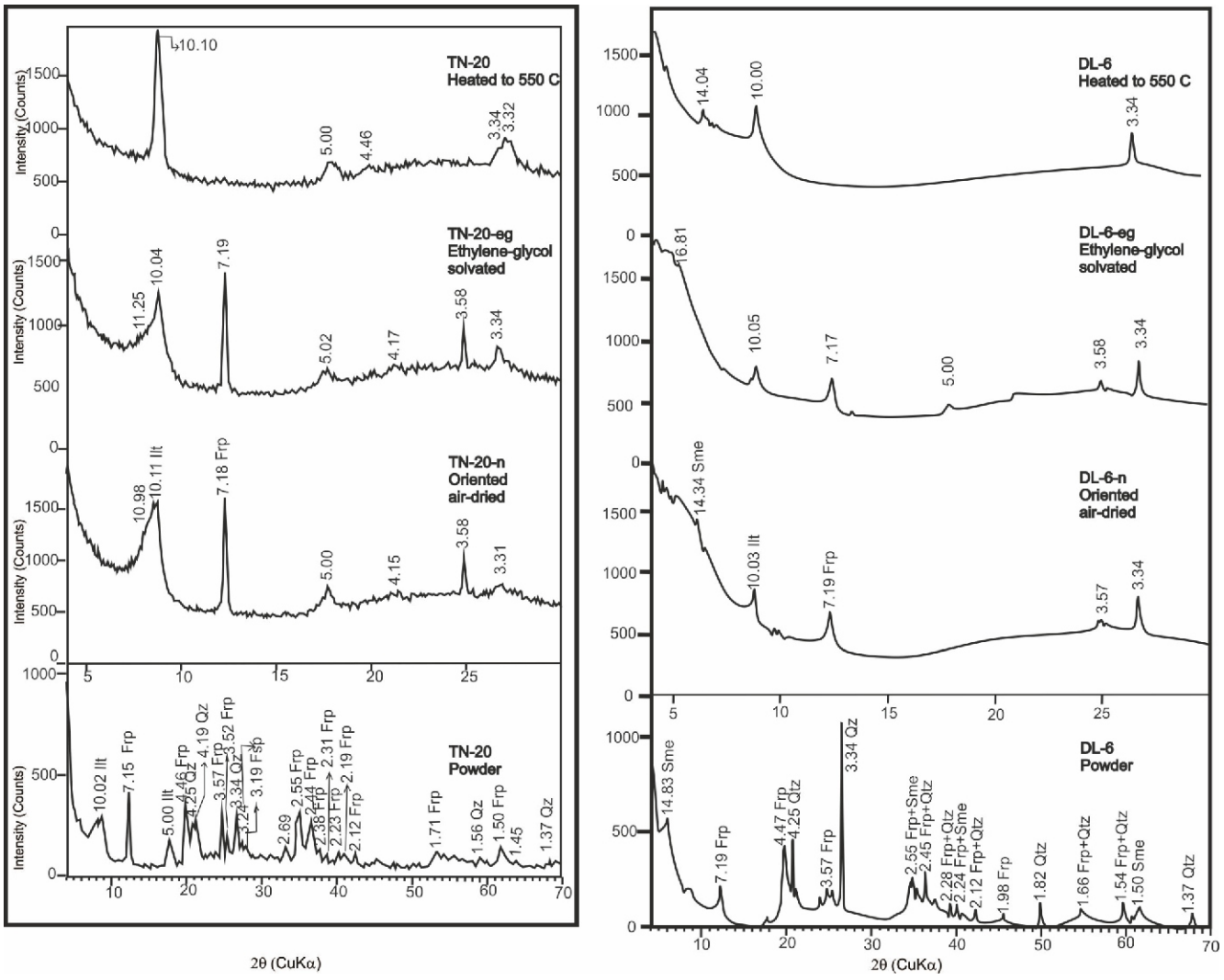

Fig. 5. X-ray diffraction patterns for clays, siltstone, gossan, cerussite and smithsonite samples taken from the Tekneli and Delikkaya Pb-Zn deposits

Explanations as in Table 1

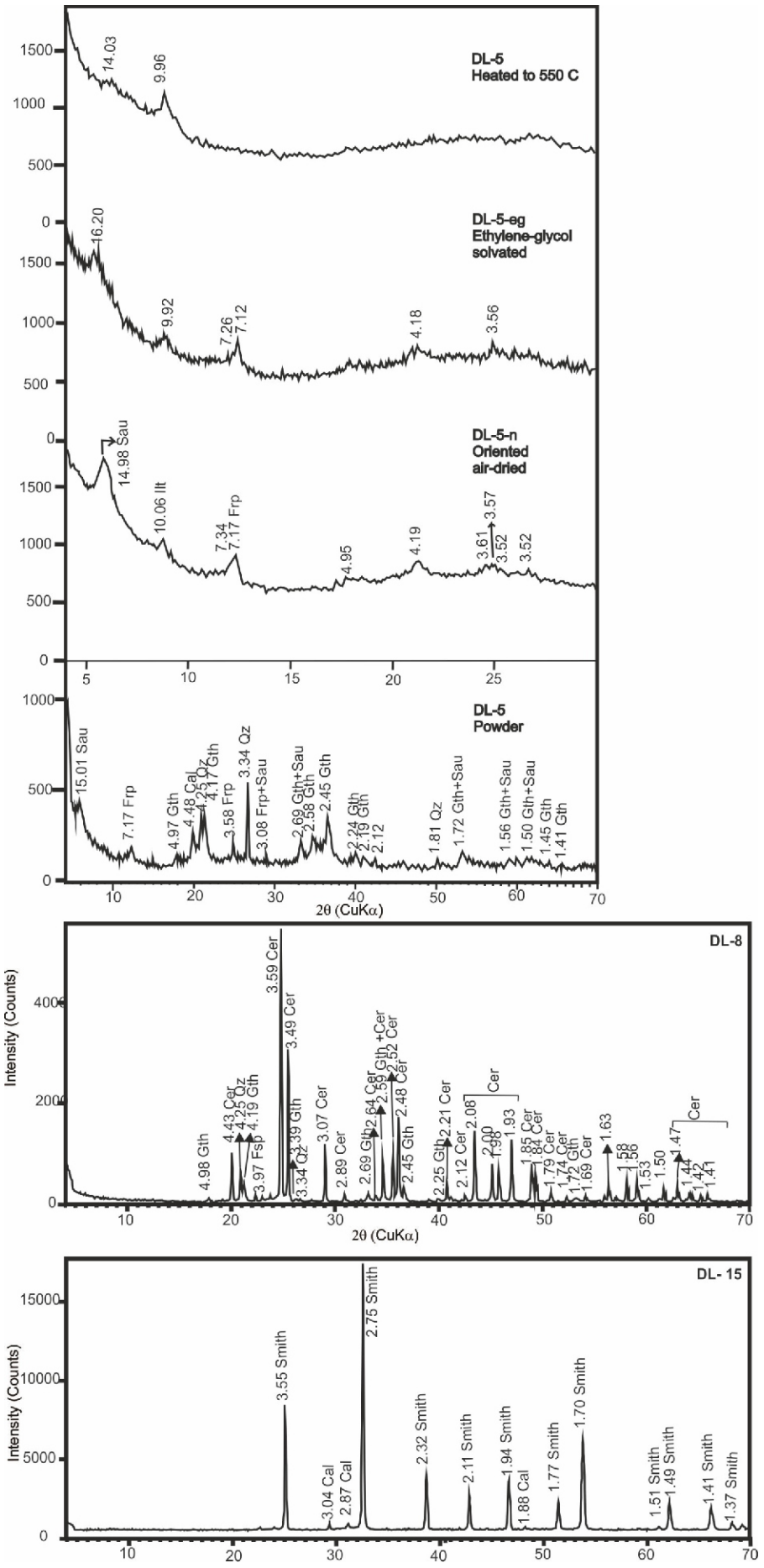
DL-5
Heated to 550 C
14.03
9.96
DL-5-eg
Ethylene-glycol
solvated
16.20
9.92
7.26
7.12
4.18
3.56
DL-5-n
Oriented
air-dried
14.98 Sau
10.06 Ilt
7.34
7.17 Frp
4.95
4.19
3.61
3.57
3.52
3.52
DL-5
Powder
15.01 Sau
7.17 Frp
4.97 Gth
4.48 Cal
4.25 Qz
4.17 Gth
3.58 Frp
3.34 Qz
3.08 Frp+Sau
2.69 Gth+Sau
2.58 Gth
2.45 Gth
2.24 Gth
2.19 Gth
2.12
1.81 Qz
1.72 Gth+Sau
1.56 Gth+Sau
1.50 Gth+Sau
1.45 Gth
1.41 Gth
2θ (CuKα)
DL-8
Intensity (Counts)
3.59 Cer
3.49 Cer
4.43 Cer
4.25 Qz
4.19 Gth
3.97 Fsp
3.39 Gth
3.34 Qz
3.07 Cer
2.89 Cer
2.69 Gth
2.64 Cer
2.59 Gth +Cer
2.52 Cer
2.48 Cer
2.45 Gth
2.25 Gth
2.21 Cer
2.12 Cer
2.08 Cer
2.00
1.98
1.93
1.85 Cer
1.84 Cer
1.79 Cer
1.74 Cer
1.72 Gth
1.69 Cer
1.63
1.58
1.56
1.53
1.50
1.47 Cer
1.44
1.42
1.41
4.98 Gth
2θ (CuKα)
DL- 15
Intensity (Counts)
3.55 Smith
2.75 Smith
3.04 Cal
2.87 Cal
2.32 Smith
2.11 Smith
1.94 Smith
1.88 Cal
1.77 Smith
1.70 Smith
1.51 Smith
1.49 Smith
1.41 Smith
1.37 Smith

Fig. 5 cont.

fraipontite (Fig. 5). The basal reflection was not affected by ethylene-glycolation, but collapsed following heating to 550°C. Sauconite was identified in one sample (DL-5) which 15.1, 3.09, 2.69, 1.72, 1.56 Å (Fig. 5). The faint smectite reflections were defined at 14.83 Å and expanded to 16.81 Å following ethylene-glycol solvation and collapsed to 10.00 Å upon heating to 550°C (Fig. 5). Illite/mica was identified by reflections at 10 Å and 5 Å in all samples, goethite/hematite and pyrite by peaks at 2.69–2.70 Å, cerussite by peaks at 4.43 and 3.59 Å and simitsonite by peaks at 3.55 and 2.75 Å (Fig. 5).

SEM-EDX DETERMINATIONS

Fraipontite crystals occur as platy outlines (Fig. 6A, B) on the edges of detrital illite and layers of this clay mineral parallel to illite. Mica alteration or partial dissolution was not observed and fraipontite was developed by nucleation and epitaxial growth on detrital illite. EDX spectra of the fraipontite shows low sharp peaks for Al (28–30%), and K (9.54%), high Si (41.64–47.79%) and Zn (12.67–14.80%; Fig. 6C, D). Sauconite was observed with lamellar structure and associated with fraipontite as filling the porosity (Fig. 6E). EDX analyses show that the sauconite is composed of Si (31.7%), Al (17.63%), Mg (10.85%), Fe (29.5%), and Zn (10.2%; Fig. 6F). The smectite exhibits a compact, flaky irregular form and is developed in voids (Fig. 6G). Star-shaped goethite/hematite crystals also developed in close association wtih fraipontite plates (Fig. 6H).

FTIR

FTIR spectra of sample DL-6 are shown in Figure 7. The weaker bands at 3697 cm^{-1} and 3623 cm^{-1} which were interpreted as Al-OH-Al stretching vibrations of smectite (beidellite) and illite, respectively (Zviagina et al., 2004; Buatier et al., 2016). The OH-bending band at 1638 cm^{-1} is related to the presence of absorbed water in the fraipontite (Koloprogge et al., 2001). The fraipontite spectra contain Si-O streching bands at 999 and 796 cm^{-1}, accompanied by Si-O-Al and Si-O-Zn bands around 688 and 463 cm^{-1}. In addition, goethite can also be identified at 796 cm^{-1} in the spectra (Buatier et al., 2016). The strong band at 530 cm^{-1} was attributed to the Zn-O vibration of fraipontite and quartz (Koloprogge et al., 2001; Buatier et al., 2016). The fraipontite shows a band at 427 cm^{-1} which is associated with the Si-O bending mode overlapping with the Zn-OH translation mode (Koloprogge et al., 2001) and the presence of goethite (Buatier et al., 2016).

ORE MINERALOGY

Galena and Fe-hydroxides, traces of sphalerite, pyrite, hematite, magnetite and rutile were detected in the polished sections (Fig. 8). Galena with max. 900 µm grain size was transformed to cerussite/anglesite and associated with Fe-hydroxides (Fig. 8A–F). Sphalerite as a main ore mineral occurs within the galena surrounded by cerussite + anglesite (Fig. 8C). Pyrite shows a pseudomorphic form, transformed to Fe-hydroxide and associated with galena (Fig. 8A, D). Fe-hydroxides exhibit anhedral, colloform and spherical forms (Fig. 8E). An accessory rutile crystal was identified in the Fe-hydroxides.

CHEMICAL ANALYSES

MAJOR ELEMENT OXIDES

Bulk chemical analyses of the parent rocks (mineralized dolomitic limestone, limestone, and non-mineralized limestone), gossan and clays are given in Table 2. Al_2O_3 (0.07 wt.%) shows depletion compared to those of values for the non-mineralized limestone, while MgO (16.67 and 0.95 wt.%) is enriched in the mineralized dolomitic limestone and limestone.

Gossan samples showed proportions of high Fe_2O_3 (64.01–75.52 wt.%) and low other major oxides compared to the clays, limestone and dolomitic limestone.

The low-moderate SiO_2 (28.06–48.53 wt.%) and low Al_2O_3 (18.05–22.55 wt.%), high Fe_2O_3 (8.27–25.50 wt.%) values in the clay samples and XRD analyses indicate the presence of Fe-bearing kaolinite and smectite. The SiO_2/Al_2O_3 ratios in the clays and limestone/dolomitic limestone range between 1.55 and 6.64. The contents of MgO (0.03–1.80 wt.%), CaO (0.12–6.46 wt.%), and Na_2O (0.01–0.52 wt.%) are lower in the clays than in the limestone and dolomitic limestone. The proportions of K_2O (3.87 wt.%) and TiO_2 (0.87–1.26) in clays were lower. A plot of SiO_2 vs. Al_2O_3 (r^2 = 0.98), Al_2O_3 vs. TiO_2 (r^2 = 0.99) and SiO_2 vs. K_2O (r^2 = 0.82) shows positive correlations while SiO_2 vs. Fe_2O_3 (r^2= –0.56) and SiO_2 vs. LOI (r^2= –0.38) show negative correlations (Fig. 9A–E). The LOI of limestones/dolomitic limestone, gossan and the clays show avg. 43.36, 13.91 and 14.52% values, respectively.

Significant enrichment and depletions of major elements were distinguished relative to major element values of Upper Continental Crust (UCC; Taylor and McLennan, 1985; Fig. 10). Generally, SiO_2, MgO, CaO, K_2O and Na_2O were depleted in the clays and gossan samples from Tekneli and Delikkaya deposits relative to UCC. Al_2O_3 and Fe_2O_3 were enriched in all samples.

TRACE ELEMENTS

There was high Ba (242 and 8 ppm), As (2.9 and 4.8 ppm), Zn (9.9 and 226 ppm) and Pb (131.5 and 2878.7 ppm) in the mineralized dolomitic limestone and limestone compared to non-mineralized limestone (Table 2). The clay samples include high Ba (max. 1056 ppm), As (max. 839.7 ppm), Cu (max. 63.4 ppm), Co (max. 40.4 ppm), Ni (max.171.6 ppm), Zr (max. 303 ppm), Zn (up to 10000 ppm) and Pb contents (max. 5152.3 ppm). High Ga (6.3–285.2), Sb (max. 54.1 ppm) and Mo (max. 133.5 ppm) were detected in the gossan (Table 2). Low U (0.1–9.2 ppm except TN-20) values were detected in all lithologies studied. The plot of Fe_2O_3 vs. each of Pb (r^2 = 0.74) and Zn (r^2 = 0.64) show positive correlations (Fig. 9F, G). The trace elements were normalized to Upper Continental Crust (UCC) values (Fig. 10; Taylor and McLennan, 1985). The UCC-normalized enhancement of transition metals (Mn, V, Co, Ni, Cu, Zn), high field-strength elements (Ti, Zr, Hf, Nb, Ta, Mo, W), alkali and alkaline earth elements (Rb, Cs), actinides and heavy metals (Pb, U) were determined in the clays and all elements were depleted (except Pb, U, and Mo) in the gossan samples from the Tekneli and Delikkaya deposits (Fig. 10).

RARE EARTH ELEMENTS (REE)

Whole-rock rare earth values of samples taken from the Tekneli and Delikkaya Pb-Zn deposits were normalized to UCC values (Fig. 10; Taylor and McLennan) and show similar patterns in spider diagrams. The average REE values of the dolomitic limestone and limestone samples are 12.83. The gossan samples from Tekneli deposit shows high REE (max. 70.36 ppm) values and high ratios of LREE/HREE (max. 39.09 ppm) relative to the Delikkaya deposit. Both the Tekneli and Delikkaya deposits show high and similar REE values and LREE/HREE ratios (162.1–247.58 and 24.73–33.11 ppm) in the clays. The light rare earth elements (LREE) [$(La/Sm)_N$ = 2.61–12.47], $(La/Yb)_N$ = 6.30–18.90] and $(La/Lu)_N$ = 6.21–31.06] were enriched and nearly flat heavy rare earth ele-

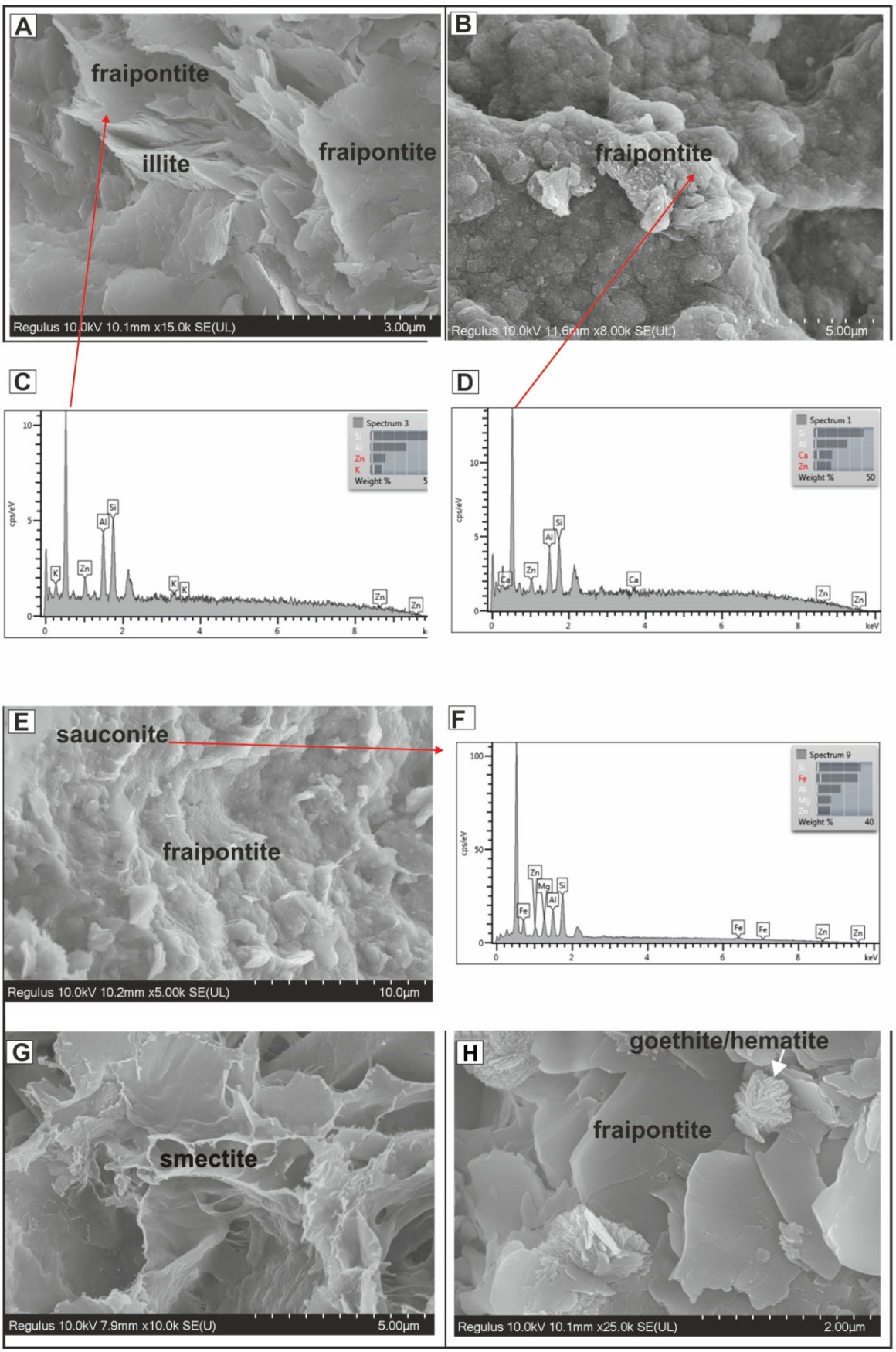

Fig. 6. SEM photographs

A – plate illite crystals edging fraipontite plates; **B** – fraipontite plates; **C**, **D** – EDX spectra of fraipontite; **E** – flaky sauconite crystals associated with fraipontite; **F** – EDX spectra of sauconite; **G** – detrital smectite in voids; **H** – star-shaped goethite/hematite on fraipontite plates

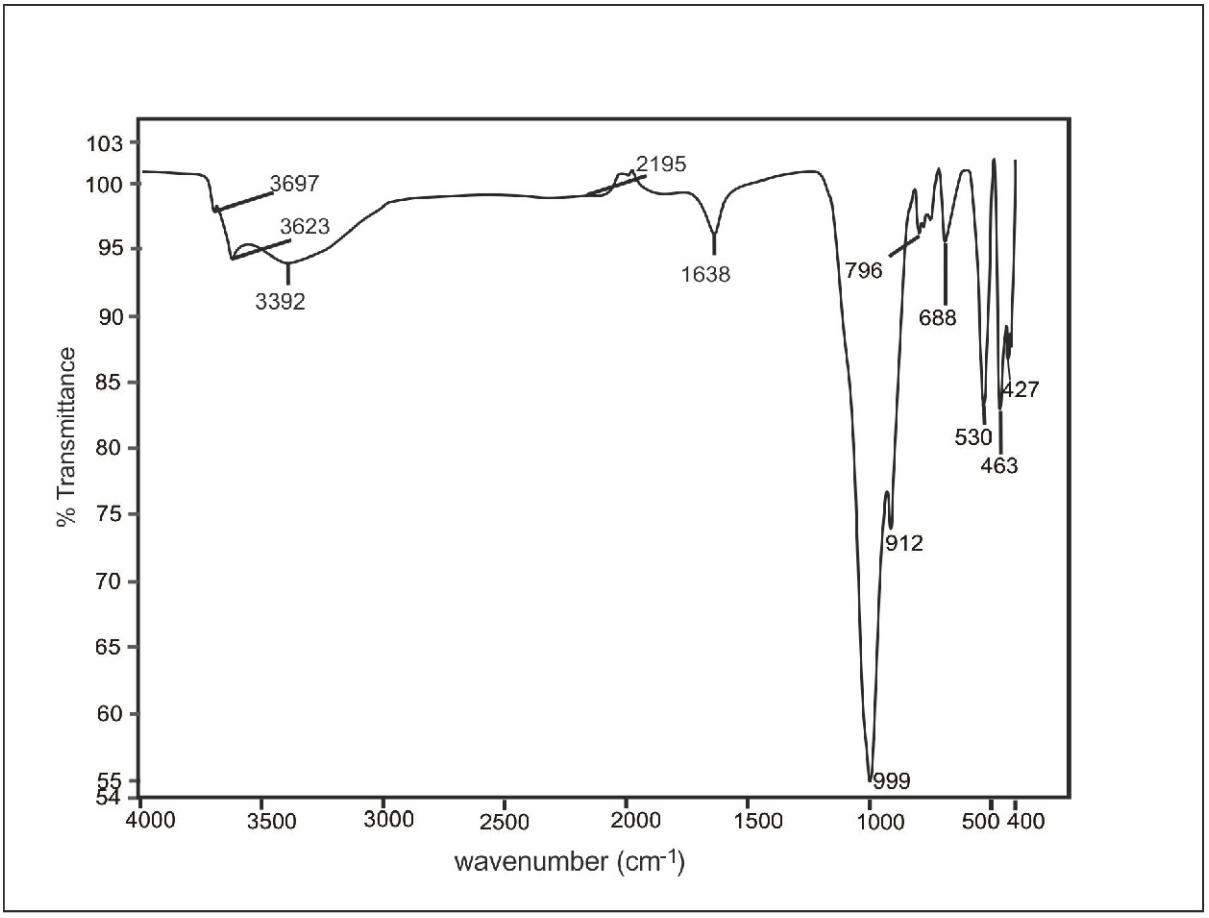

Fig. 7. IR spectra of a fraipontite sample in the study area

ments (HREE) $[Gd/Yb)_N$ = 0.01–2.99] similar to UCC rocks (Table 2). Negative Eu (0.59–0.78; except TN-3, DL-1) and negative/positive Ce (0.42–1.35) anomalies were determined in the clay, gossan and dolomitic limestone and limestone samples.

The clay samples from Tekneli and Delikkaya deposits showed enrichments of La, Ce, Nd, Ce, Sm, Eu and Gd, and depletion of Tb, Dy, Ho, Er, Tm, Yb and Lu relative to UCC (Fig. 10). The gossan samples show low values of LREE, MREE and HREE relative to UCC.

DISCUSSION

THE OCCURRENCE OF CLAY MINERALS

Non-sulphide ore consisting of smithsonite, cerussite/anglesite, goethite, hematite, residual red clays (illite, smectite) and Zn clays (fraipontite and sauconite) in the karstic cavities of uppermost Permian and Jurassic limestone/dolomitic limestone formed during oxidation of primary sulphides (galena, sphalerite, pyrite) in a supergene setting within collisional orogenic fold-fault systems in three successive stages (Fig. 11):

Stage I (Primary ore stage): the Permian and Jurassic carbonates of this study were deposited in a shallow marine environment of the Tauride belt, part of the Alpine-Himalayan orogenic belt, with subsequent collapse of the carbonate platform by block faulting followed by nappe devolopment from the Late Cretaceous to the Eocene (Tekeli, 1980; Hanilçi and Öztürk, 2011). This stage is characterised by the formation of sphalerite, galena, and minor amounts of calcite gangue; these primary sulphides may be related to seawater saturated in metal-bearing hydrothermal fluids after limestone sedimentation (Fig. 1A; Tekeli et al., 1983), so favouring the formation of1 the Tekneli and Delikkaya MVT deposits from the Late Cretaceous to the Paleocene, in a similar way to the Magellan MVT Pb deposit (Pirajno et al., 2010; Hanilçi and Öztürk, 2011).

Stage II (oxidation stage): this stage consists of goethite, hematite, smithsonite, anglesite and cerussite (Fig. 11B). Furthermore, this stage was associated with several uplift and weathering processes between Miocene and recent times in the study area and the development of strike-slip and normal faults (Hanilçi and Öztürk, 2011). The uplift of the Permian-Jurassic carbonate platform and downward percolation of meteoric waters caused oxidation of the sulphides which led to pH decrease and accelerated karstification, dissolving the Permian-Jurassic limestone/dolomitic limestone with resulting development of karst features (Hanilçi and Öztürk, 2011; McGuire, 2012; Kahya et al., 2019; Garnit et al., 2022). The hematite formed under neutral pH conditions, while goethite was formed in early acidic conditions (Jönsson et al., 2006). The galena transformed to anglesite, followed by cerussite that occurred around the galena at low pH in the oxidation zone below the leaching zone, because of lead being more immobile relative to Zn (Sangameshar and Barnes, 1983; Poot et al., 2020). If the Zn-Pb sulphate solutions interact with limestone/dolomitic limestone under pH>7 and high partial pressure of $(CO_2)g$,

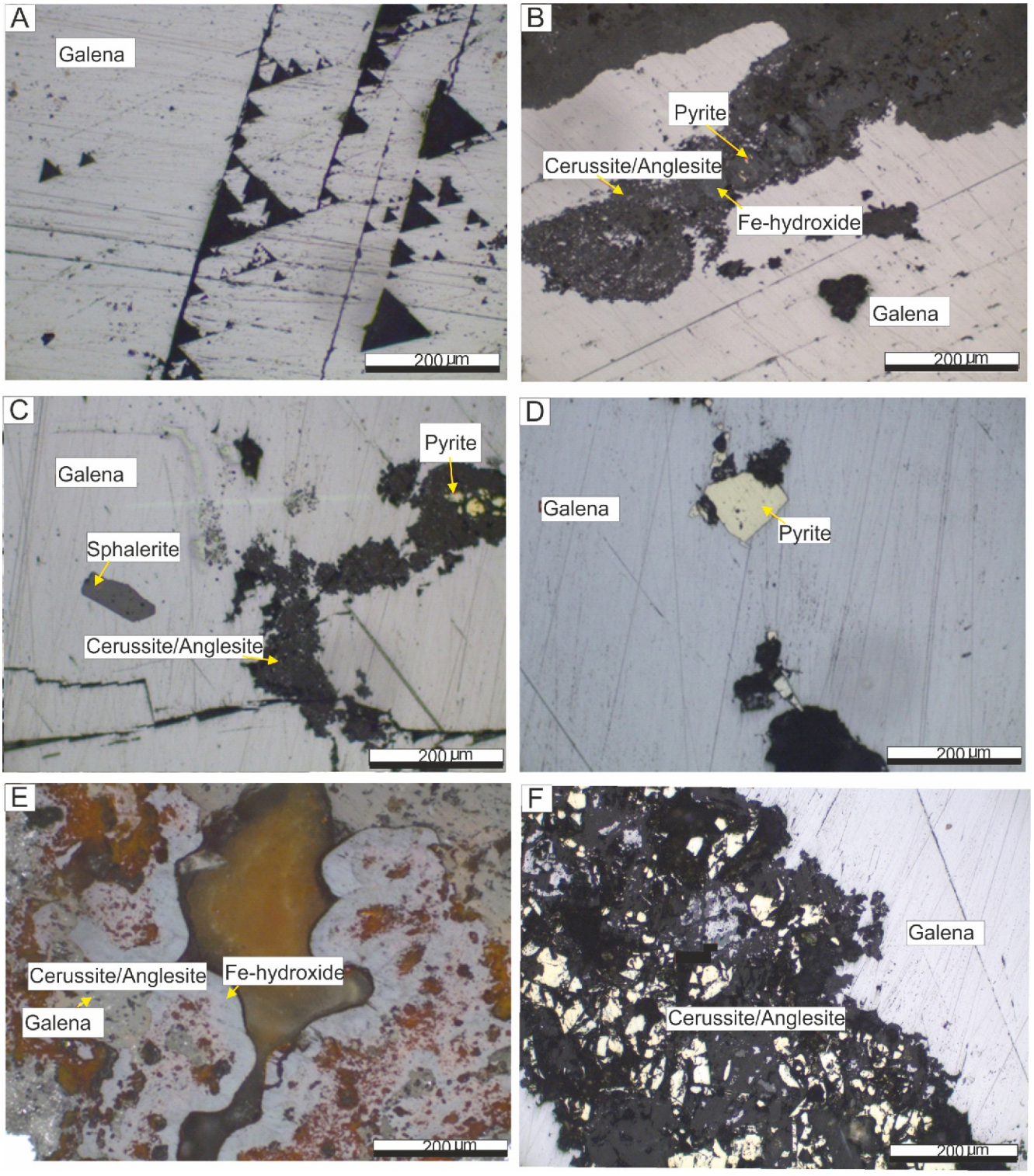

Fig. 8A, B – galena associated with cerussite/anglesite and Fe-hydroxides; C – relic sphalerite within galena and associated with cerussite /anglesite; D – pyrite pseudomorph; E – colloform Fe-hydroxides around galena; F – galena with cerussite /anglesite

Table 2

Major- (wt.%) and trace-element (ppm) compositions of fresh and altered rocks from the study area (see Table 1 for the mineralogical compositions of the samples)

	Mineralized dolomitic limestone	Mineralized limestone	Non-mineralized limestone	Gossan			
Major oxides (wt.%)	TN-5	TN-8	TN-24	TN-3	TN-23	DL-1	TN-13
SiO_2	5.18	2.22	0.24	3.99	2.79	4.95	7.93
Al_2O_3	0.78	0.60	0.07	2.69	0.91	1.83	3.34
Fe_2O_3	0.65	0.31	0.21	75.99	72.64	74.06	69.61
MgO	16.67	0.95	0.49	0.13	0.04	0.10	0.19
CaO	32.03	52.73	55.73	0.15	0.12	0.20	0.24
Na_2O	0.03	<0.01	<0.01	<0.01	<0.01	<0.01	<0.01
K_2O	0.13	0.10	<0.01	0.23	0.13	0.30	0.36
TiO_2	0.05	0.03	<0.01	0.12	0.07	0.34	0.14
P_2O_5	0.01	0.01	<0.01	0.01	0.14	0.20	0.13
MnO	0.01	0.01	<0.01	0.03	<0.01	<0.01	0.03
Cr_2O_3	0.022	0.004	0.003	0.026	0.013	0.012	0.017
TS	0.05	0.25	<0.02	0.05	0.12	0.12	<0.02
TOC	11.53	11.46	11.78	0.20	0.62	0.20	0.27
LOI	44.3	42.6	43.2	13.7	11.6	14.0	14.5
Total	99.85	99.58	99.95	97.15	88.47	95.99	96.48
Ba	242	8	2	19	22	23	19
Cr	6.1	1.1	0.8	7.2	3.6	3.3	4.7
Co	1.8	0.7	<0.2	3.8	1.2	0.6	13.3
Cs	0.3	0.2	<0.1	0.8	1.0	1.9	3.1
Ga	<0.5	0.8	<0.5	13.4	124.5	31.8	6.3
Hf	0.6	0.2	<0.1	0.7	0.4	1.6	0.8
Nb	1.0	0.8	<0.1	2.9	1.3	6.1	2.8
Rb	5.1	4.3	0.6	9.7	7.2	15.7	16.0
Sn	<1	<1	<1	<1	3	1	<1
Sr	200.1	552.0	114.8	15.3	11.9	42.5	10.9
Ta	<0.1	<0.1	<0.1	0.2	<0.1	0.4	0.2
Th	1.2	0.4	<0.2	1.8	0,5	2.4	2.4
U	3.1	1.4	0.6	12.9	5.1	8.9	8.5
V	9	14	<8	139	107	164	145
W	<0.5	<0.5	<0.5	1.4	<0.5	0.8	0.7
Zr	24.4	7.5	1.1	28.4	13.4	64.3	32.8
Y	4.0	2.0	1.0	8.3	0.7	5.5	18.2
La	2.9	2.2	0.8	6.8	2.9	9.2	15.5
Ce	6.4	4.1	1.7	11.2	3.7	10.3	16.5
Pr	0.79	0.47	0.20	1.50	0.41	1.69	4.40
Nd	4.0	1.8	0.7	5.7	1.2	5.9	17.6
Sm	0.69	0.36	0.16	1.12	0.15	0.97	3.82
Eu	0.15	0.07	0.04	0.21	0.03	0.22	0.88
Gd	0.74	0.33	0.16	1.15	0.10	0.89	3.69
Tb	0.11	0.05	0.02	0.17	0.01	0.14	0.58
Dy	0.6	0.30	0.13	1.07	0.10	0.87	3.08
Ho	0.13	0.06	0.03	0.23	<0.02	0.18	0.63
Er	0.37	0.18	0.08	0.67	0.08	0.56	1.72
Tm	0.05	0.02	0.01	0.09	0.01	0.09	0.23
Yb	0.33	0.14	<0.05	0.55	0.11	0.58	1.52
Lu	0.05	0.02	<0.01	0.09	0.01	0.09	0.21
Pb	131.5	2878.7	88.0	2533.7	>10000	7176.0	5534.0
Zn	99	226	26	>10000	>10000	>10000	>10000
Ni	26.4	7.7	3.8	106.1	30.0	16.3	119.5

Tabl. 2 cont.

	Mineralized dolomitic limestone	Mineralized limestone	Non-mineralized limestone	Gossan			
Major oxides (wt.%)	TN-5	TN-8	TN-24	TN-3	TN-23	DL-1	TN-13
Au (ppb)	<0.5	<0.5	<0.5	0.9	1.1	2.2	0.7
Ag	<0.1	0.6	<0.1	0.5	1.3	6.1	1.5
Mo	2.0	1.9	0.4	133.5	39.0	57.2	34.3
Cu	1.7	1.1	0.4	16.9	25.8	12.9	17.2
As	4.8	2.9	0.8	181.4	617.6	55.0	180.5
Cd	0.7	1.1	0.3	22.9	71.7	54.7	58.2
Sb	0.3	0.6	0.3	12.1	27.5	4.5	4.0
Hg	0.01	0.03	<0.01	0.04	0.41	0.15	0.03
REE	21.31	12.1	5.09	38.85	9.53	37.18	70.36
LREE/ HREE	17.61	23.80	22.6	18.07	39.09	20.52	14.67
Eu/Eu*	0.64	0.62	0.78	2.8	0.75	3.57	0.71
Ce/Ce*	0.94	0.89	1.01	0.78	0.67	0.55	0.48
$(La/Sm)_N$	2.71	9.28	3.22	3.91	12.47	6.12	2.61
$(La/Yb)_N$	6.30	11.2	11.45	8.86	18.90	11.37	7.31
$(La/Lu)_N$	6.21	11.78	8.55	8.09	31.06	10.95	7.91
$(Gd/Yb)_N$	1.85	1.95	2.99	1.73	0.76	1.27	2.00

	Gossan				Clays							
Major oxides (wt.%)	DL-5	DL-14	DL-9	Ave.	TN-16	TN-17	TN-20	TN-21	DL-3	DL-6	DL-11	Ave.
SiO_2	3.46	3.21	3.93	4.32	28.06	41.23	35.48	41.91	48.53	44.12	44.16	40.49
Al_2O_3	1.14	0.62	1.63	1.73	18.05	23.04	22.51	21.40	20.64	20.50	22.55	21.24
Fe_2O_3	70.27	75.52	64.01	71.72	25.50	10.48	22.02	8.27	9.57	9.24	9.58	13.52
MgO	0.16	0.03	0.15	0.11	1.20	1.80	1.14	1.63	1.47	1.67	1.79	1.52
CaO	0.19	0.12	0.24	0.18	3.91	3.32	0.64	6.46	0.84	1.09	1.02	2.46
Na_2O	<0.01	<0.01	<0.01	0.01	0.03	0.05	0.52	0.04	0.06	0.04	0.04	0.11
K_2O	0.56	0.07	0.06	0.24	1.39	1.61	3.87	1.38	2.38	1.55	1.83	2.00
TiO_2	0.05	0.05	0.07	0.12	0.87	1.17	1.26	1.02	1.01	0.97	1.02	1.04
P_2O_5	0.12	0.05	0.14	0.11	0.26	0.14	0.06	0.13	0.13	0.14	0.17	0.13
MnO	0.05	0.03	0.02	0.03	0.25	0.15	0.03	0.19	0.10	0.18	0.08	0.14
Cr_2O_3	0.007	0.008	0.007	0.01	0.028	0.028	0.027	0.021	0.023	0.021	0.022	0.02
TS	1.16	0.06	0.10	0.21	<0.02	<0.02	0.05	<0.02	0.03	0.04	0.03	0.03
TOC	0.36	0.37	0.87	0.41	0.81	0.60	0.45	1.21	0.17	0.12	0.15	0.50
LOI	17.2	14.1	12.3	13.91	15.8	15.5	11.9	16.9	12.3	14.6	14.7	14.52
Total	93.21	93.79	82.52	92.51	95.36	98.59	99.47	99.48	97.10	94.11	97.03	97.30
Ba	13	12	32	20	155	290	232	1056	281	236	256	358
Cr	1.9	2.2	1.9	3.54	7.8	7.8	7.5	5.8	6.4	5.8	6.1	6.74
Co	3.6	<0.2	2.0	3.52	33.3	25.8	40.4	23.3	24.2	24.5	24.3	27.97
Cs	0.7	0.5	0.7	1.24	13.1	12.8	8.6	9.1	17.5	9.5	11.4	11.71
Ga	285.2	9.8	12.7	69.1	43.1	25.2	22.0	20.6	24.1	25.2	25.2	26.48
Hf	0.3	0.2	0.4	0.62	5.4	6.5	6.6	7.8	5.5	5.2	5.3	6.04
Nb	0.9	0.9	2.0	2.41	17.5	23.5	26.9	21.9	19.4	18.8	20.5	21.21
Rb	12.5	3.2	7.5	10.25	84.2	100.2	125.1	80.6	127.4	109.8	123.9	107.31
Sn	3	<1	3	1.85	3	3	4	2	4	3	3	3.14
Sr	19.0	5.9	21.1	18.08	71.8	113.3	160.5	79.8	134.2	172,8	183.7	130.87
Ta	<0.1	<0.1	0.1	0.17	1.1	1.4	1.9	1.4	1.4	1.3	1.5	1.42
Th	0.9	0.4	1.1	1.35	16.1	16.0	17.9	18.7	16.9	16.2	18.4	17.17
U	2.4	7.9	4.1	7.11	9.2	6.8	27.2	8.7	6.3	5.9	6.5	10.08
V	86	57	100	114	456	244	350	167	216	173	187	256.14
W	<0.5	<0.5	0.9	0.75	1.7	2.5	1.7	1.7	1.9	2.1	2.2	1.97
Zr	10.1	9.2	15.2	24.77	217.1	255.2	249.2	303.0	215.2	199.2	206.4	235.04
Y	6.3	1.4	5.6	6.57	19.5	21.7	14.3	28.3	14.2	22.3	27.7	21.14
La	5.7	1.6	6.7	6.91	29.4	32.4	39.3	44.0	29.9	41.1	52.5	38.37
Ce	6.3	1.7	5.9	7.94	82.2	88.0	65.2	92.1	77.4	75.8	86.2	80.98
Pr	1.21	0.29	1.51	1.57	6.33	6.38	7.02	9.60	5.89	8.39	11.19	7.82

Tabl. 2 cont.

	Gossan				Clays							
Major oxides (wt.%)	DL-5	DL-14	DL-9	Ave.	TN-16	TN-17	TN-20	TN-21	DL-3	DL-6	DL-11	Ave.
Nd	4.9	0.8	5.6	5.97	22.8	23.5	22.8	35.8	20.6	30.7	41.0	28.17
Sm	1.10	0.14	1.02	1.18	4.77	4.48	2.91	6.72	3.61	5.41	7.47	5.05
Eu	0.25	0.03	0.23	0.26	1.10	0.96	0.49	1.44	0.69	1.29	1.60	4.34
Gd	1.02	0.15	0.91	1.13	4.44	4.15	2.06	6.10	2.78	4.68	6.19	4.34
Tb	0.15	0.02	0.13	0.17	0.72	0.70	0.34	0.94	0.44	0.71	0.91	0.68
Dy	0.84	0.14	0.87	0.99	4.30	4.12	2.40	5.51	2.62	4.16	5.21	4.02
Ho	0.18	0.04	0.17	0.20	0.82	0.87	0.57	1.10	0.54	0.85	0.98	0.81
Er	0.51	0.12	0.46	0.58	2.50	2.48	1.83	3.16	1.65	2.54	2.97	2.44
Tm	0.07	0.01	0.06	0.08	0.37	0.37	0.32	0.48	0.27	0.35	0.42	0.36
Yb	0.47	0.11	0.43	0.58	2.45	2.59	2.22	3.17	1.83	2.41	2.81	2.49
Lu	0.07	0.02	0.06	0.07	0.37	0.41	0.34	0.51	0.29	0.38	0.43	0.39
Pb	>10000	4244.6	>10000	7069.75	4787.0	1969.5	100.2	687.5	1675.4	2925.7	5152.3	2471.0
Zn	>10000	>10000	>10000	10000	>10000	7569	2365	1885	>10000	>10000	>10000	7402.7
Ni	24.6	14.9	18.1	47.07	134.8	171.6	104.6	72.0	120.0	120.0	130.6	121.94
Au (ppb)	1.8	1.5	0.9	1.3	<0.5	1.2	1.4	0.5	2.1	1.8	3.1	1.51
Ag	92.9	2.8	1.2	15.18	1.3	0.3	<0.1	0.2	14.2	6.4	3.2	3.67
Mo	61.7	54.2	22.7	57.51	24.0	5.1	73.7	4.4	14.4	7.1	6.4	19.3
Cu	9.0	5.0	9.8	13.8	63.4	45.3	37.1	33.8	42.8	42.2	43.3	43.98
As	558.9	19.4	169.6	254.62	839.7	134.6	205.6	53.6	35.3	46.8	51.2	195.52
Cd	112.5	47.7	79.3	63.85	76.8	4.8	1.6	3.5	23.9	71.4	23.7	29.38
Sb	38.4	3.5	54.1	21.15	18.5	0.7	0.7	0.3	0.8	0.8	0.7	3.21
Hg	1.52	0.16	0.89	0.45	0.09	0.06	0.18	0.05	0.37	0.16	0.16	0.15
REE	29.07	6.57	29.65	31.60	182.07	193.11	162.1	238.93	162.71	201.07	247.58	198.22
LREE/ HREE	16.17	16.88	19.51	20.70	24.73	25.69	28.51	24.79	33.11	27.46	28.79	27.58
Eu/Eu*	0.72	0.62	0.72	1.22	0.73	0.68	0.61	0.68	0.66	0.78	0.59	0.67
Ce/Ce*	0.52	0.54	0.42	0.56	1.35	1.33	0.84	1.0	1.27	0.9	0.79	1.06
$(La/Sm)_N$	3.34	7.37	4.24	5.72	3.97	4.66	8.71	4.22	5.34	4.90	4.53	5.19
$(La/Yb)_N$	8.69	10.43	11.17	10.96	8.60	8.97	12.69	9.95	11.71	12.23	13.40	11.07
$(La/Lu)_N$	8.72	8.57	11.96	12.46	8.51	8.46	12.38	9.24	11.04	11.59	13.08	10.61
$(Gd/Yb)_N$	1.79	1.14	1.75	1.49	1.49	1.32	0.76	1.59	0.01	1.60	1.82	1.22

REE = the sum of (La–Lu)+Y; LREE = the sum of La–Nd; MREE = the sum of (Sm–Ho); HREE = the sum of (Er–Lu); $Eu/Eu^*=Eu_N/?(Sm_N*Gd_N)$ and $Ce/Ce^*=3Ce_N/(2La_N+Nd_N)$ (Mongelli, 1997), where N refers to a chondrite compositions normalized value (Taylor and McLennan, 1985)

smithsonite and cerussite may be formed. Furthermore, the high mobile Zn ions may be transported over long distances, and thus smithsonite was found in every part of the ore body in the study area (Choulet et al., 2014).

Stage III (supergene enrichment stage): the karst cavities are filled with argillaceous materials (Fe-rich residual clays) and oxidised ores (smithsonite, cerussite, hematite and goethite) were transported to karst caves as breccia matrices by groundwater after limestone dissolution (Fig. 11C ; Iacoviello and Martini, 2013; Garnit et al., 2022). The detrital materials originated from ophiolitic, Permian-Jurassic carbonate rocks, and Triassic siliciclastic strata (mudstone, siltstone, and marl) in the study area. The red clay type of the residual clays (illite and smectite) consist of mixed components from both detrital sources (feldspar, muscovite, chlorite) and insoluble limestone materials (Chamley, 1989) similar to the salt domes of the Tunisian Zn-Pb deposit (Bechtel et al., 1999), and southern Belgian (De Putter et al. 2002), and Sardinian non-sulphide mineralization (Boni and Mondillo, 2015). The clay within the study area is usually iron-stained and located either in karstic cavities in the upper part of the deposit or as thin laminated clay-Fe-(oxyhydr)oxide infills. Zn clays (fraipontite and sauconite) developed on detrital illite/mica based on SEM data in the study area, indicating that these clays occurred authigenically by partial dissolution of outer illite/mica layers, hydrolysis and breaking of Al-Si-O bonds supplying the Al and Si, then direct precipitation of Zn clays in open spaces during supergene processes and local contribution of hydrothermal fluids similar to the phenomena reported by Choulet et al. (2016), Buatier et al. (2016) and Balossone et al. (2017). The absence of kaolinite (except in the mudstone and siltstone) in the study area, based on XRD data, suggests that the kaolinite dissolved and provided Al for the Zn clays, remaining in meteoric waters due to the low mobility of Al, and providing a source similar to that of the zinc clays of the Bou Arhous deposit in the Moroccan High Atlas (Choulet et al., 2016). The source of Zn was sphalerite, Zn-rich solutions being retained in groundwater during the supergene stage leading to formation of Zn clays (Boni et al., 2009).

MINERALOGICAL IDENTIFICATION FROM PARENT ROCK SAMPLES

The monomineralic, subrounded quartz clasts in thin sections from the study area shows a detrital origin, transported and deposited in the limestone/dolomitic limestone during early silicification similar to the process reported by Zhou et al. (2023). In addition, the presence of accessory chlorite, mica

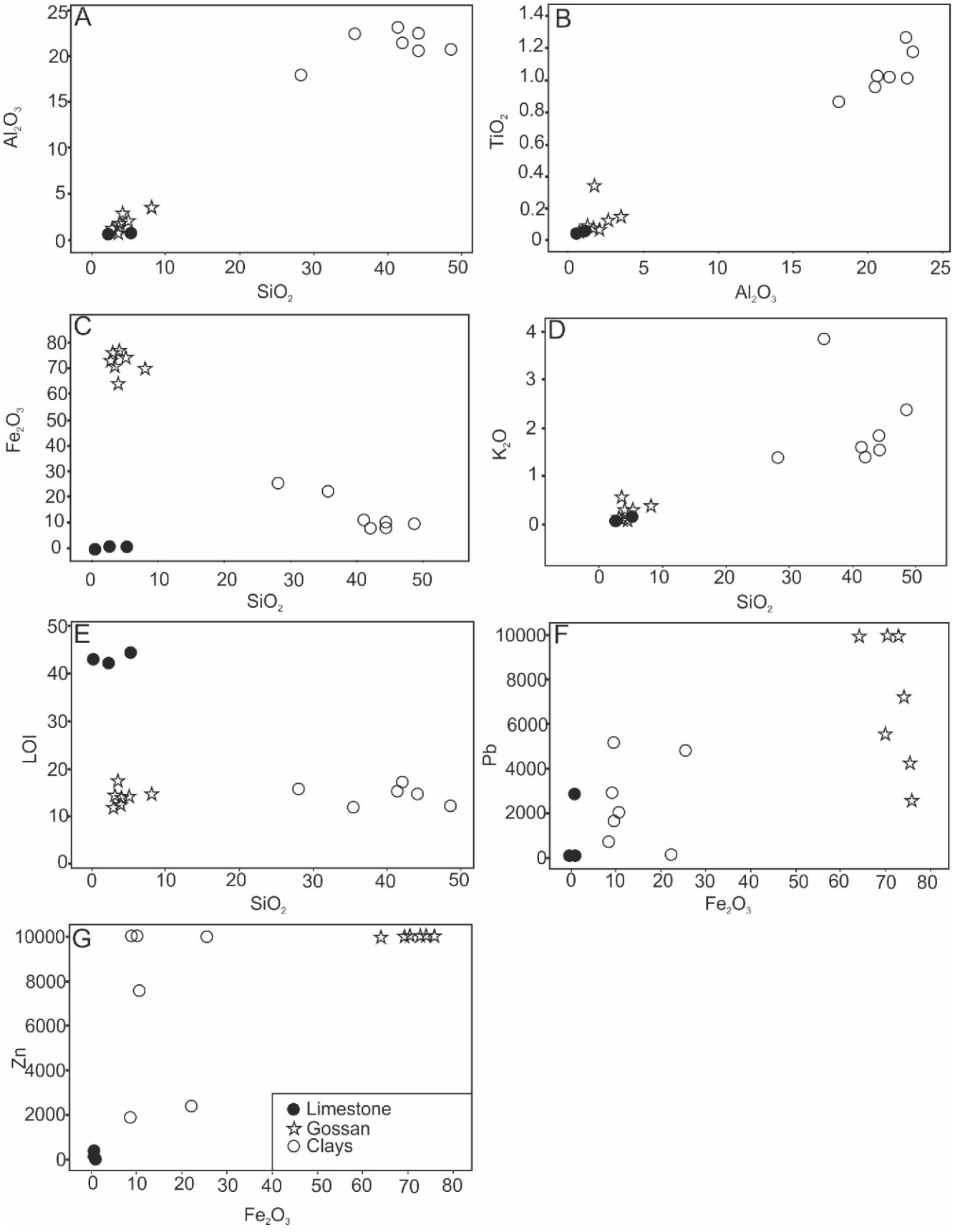

Fig. 9. Element variation diagrams for major oxides (wt.%) and trace elements (ppm) of the Tekneli and Delikkaya limestone, gossan and clay samples

A – Al_2O_3 vs. SiO_2; **B** – TiO_2 vs. Al_2O_3; **C** – Fe_2O_3 vs. SiO_2; **D** – K_2O vs. SiO_2; **E** – LOI vs. SiO_2; **F** – Pb vs. Fe_2O_3; **G** – Zn vs. Fe_2O_3

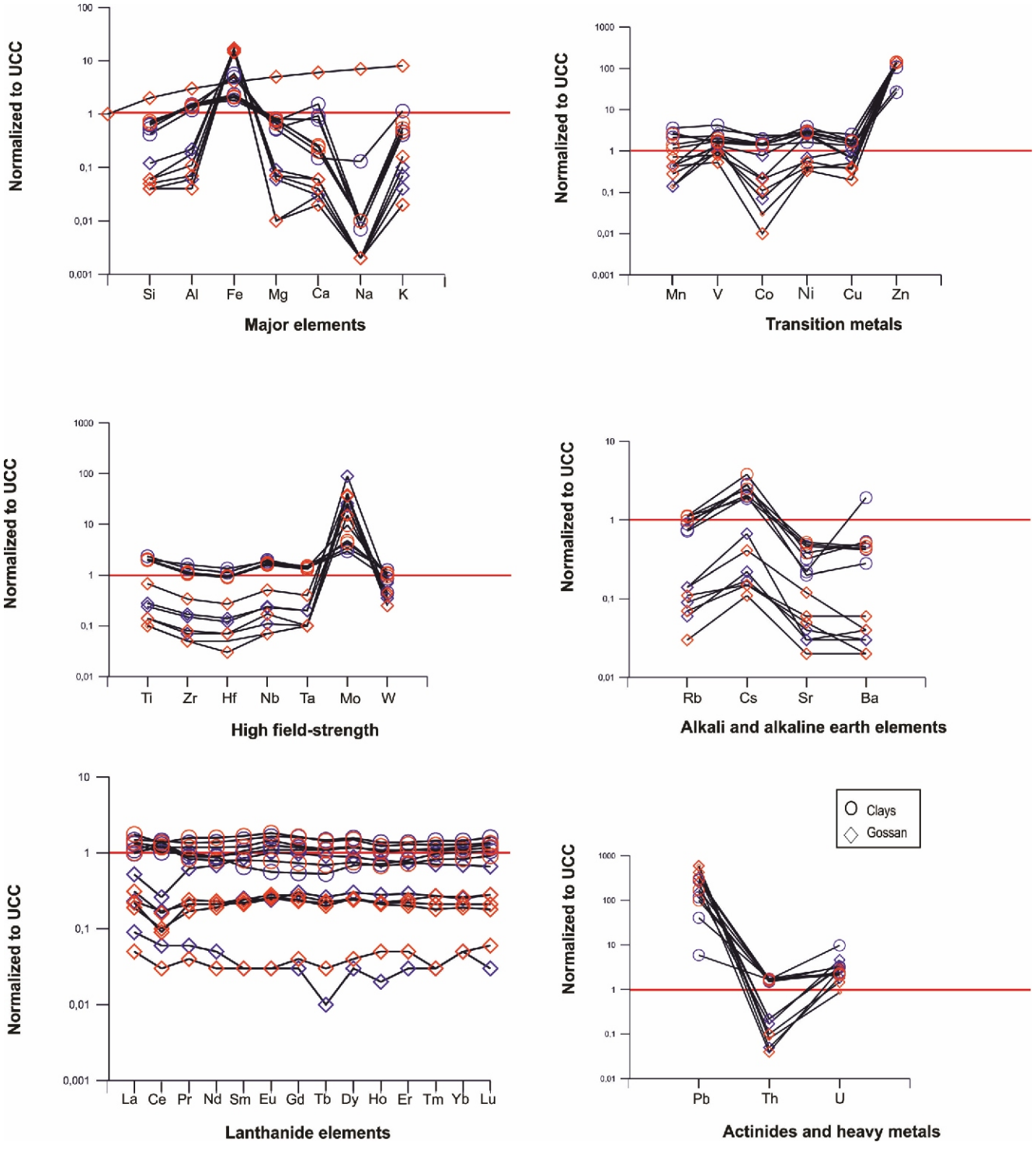

Fig. 10. Plots of major elements, transition metals, high field-strength elements, alkali and alkaline earth elements, lanthanide elements, and actinides and heavy metals from gossan and clay samples from the Tekneli (blue symbols) and Delikkaya (red symbols) Pb-Zn deposits normalized to UCC of Taylor and McLennan (1985)

and amphibole, and decrease of feldspar in the limestone/dolomitic limestone, clay and gossan samples suggest a detrital origin similar to that of the detrital clays in the Bursa-Orhaneli coal deposit (Erkoyun et al., 2022). The smithsonite, hematite, goethite, clay minerals and calcite were formed in supergene alteration facies similar to that of the carbonated-hosted MVT Zn-Pb deposits in Behabad-Iran (Parsa and Magsudi, 2018). Hanilçi and Öztürk (2011) also described kaolinite, quartz and pyrite in the Çadırkaya (Yahyalı) Pb-Zn deposit of the Aladağlar region.

The fraipontite was characterized by XRD peaks and typical IR spectroscopy bands in the study area, as in the studies reported by Kloprogge et al. (2001), Choulet et al. (2016) and Buatier et al. (2016). Sauconite was identified by XRD peaks

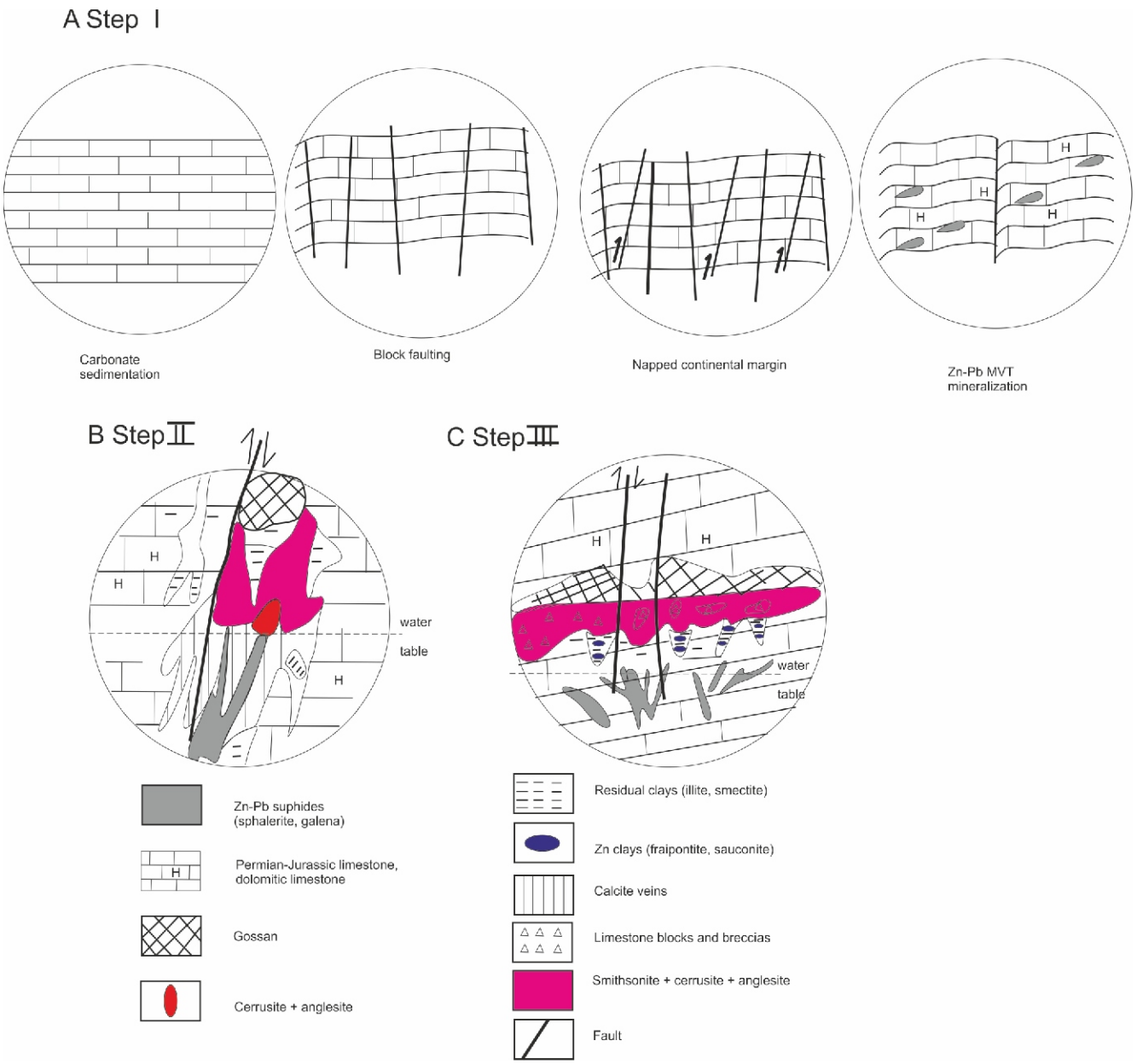

Fig. 11. Genetic model of the Tekneli and Delikkaya deposits

A – stage I (primary ore stage); **B** – Stage II (oxidation stage); **C** –Stage III (supergene enrichment stage)

and locally mixed with fraipontite similar to that in the Mina Grande zinc deposit (Norhern Peru; Arfè et al., 2017). Detrital smectite was developed irregularly in cavities based on SEM studies, and mixed with detrital illite and small amounts of fraipontite according to XRD data (Buatier et al., 2016).

GEOCHEMICAL EVIDENCE FROM MAJOR OXIDES AND TRACE ELEMENTS OF THE CLAY AND HOST ROCK SAMPLES

The positive correlation of SiO_2 vs. Al_2O_3 and K_2O, negative correlation between SiO_2 and LOI are related to the high silicilastic component of the samples (Fig. 9) similar to those in the Peru Cu-Zn deposit (Escalante et al., 2010). Furthermore, the high contents of SiO_2, Al_2O_3 and Fe_2O_3 support an allochthonous source supplying silicate material (Micheletti et al., 2023). The positive correlation of Al_2O_3 vs. TiO_2 may be related to the abundance of detrital material such as siltstone, mudstone, marl, limestones/dolomitic limestone, and clay inputs, with a felsic source similar to those reported by Akinyemi et al. (2013) and Okonkwo and Okunlola, 2022. Furthermore, the increase of LOI in the clays (ave. 14.52%) and Al (ave. 21.24%) values suggest the presence of aluminium silicate minerals (Micheletti et al., 2023).

SEM-EDX analyses of the fraipontite show Zn, Al and Si enrichment relative to sauconite similar to that reported by Buatier et al. (2016) and always texturally related to illite based on the K concentration in the fraipontite of the study area, similarly to Zn clays in the Cristal and Mina Grande zinc deposits (Northern Peru; Arfè et al., 2017).

The negative correlation of SiO_2 vs. Fe_2O_3 and high Fe_2O_3 (up to 75.52%) values of the gossan samples indicate that iron was not removed by supergene fluids in the upper part of the Tekneli and Delikkaya Pb-Zn deposits (Verhaert et al., 2017). This gossan zone was developed by the oxidation and alter-

ation of pyrite under arid conditions, associated with Al, and locally K-, Na- or Mg-bearing minerals similar to those in the north Greenland Zn-Pb deposit along a fault zone (Pour et al., 2018).

The UCC-normalized major elements show depletion of mobile elements (Si, Mg, Na, Ca and K) into solution, and enrichment of immobile elements (Al and Fe) in clays, suggesting the loss of feldspars during enhanced chemical weathering in a hot and humid climate (Wronkiewicz and Condie, 1987; Rahman et al., 2020; Wu et al., 2023).

The significant amount of As in the clays related to As is incorporated into the structure of Fe oxides (goethite), suggesting that enrichment of Fe oxide contents in clays as shown by SEM data in the study area is similar to that of the Olkusz MVT deposit (Poland; Jerzykowska et al., 2014). The enrichment of Cr, Co and Ni in the clays is likely related to a detrital contribution from ophiolitic rocks in the study area. The enhancement of Ni, V, Fe and Co in the clays relative to UCC resulted in substitution between Fe and Ni, Co and V, and precipitation in Fe oxides (Rahman and Suzuki, 2007; Kadir et al., 2015; Jiang et al., 2016; Helvacı et al., 2018). The clay samples are characterized by high Zn and Pb values in the Tekneli and Delikkaya deposits due to the Zn^{+2} cation location at the clay surface or in the interlayer similar to those reported for karst-filled Zn clays in the non-sulphide Bou Arhous Zn-Pb deposit of Morocco (Choulet et al., 2016).

The low U values (<10 ppm), though enriched relative to UCC, in the gossan and clay samples are related to oxic conditions similar to those of the MVT Pb-Zn-Ag deposit in Germany-Wiesloch (Pfaff et al., 2009) and the U may be adsorbed onto clay minerals (Dong et al., 2012). The high Zr values in the clays are related to Zr immobility during weathering and precipitated within mudstone and siltstone and transported to clays (Dypvik and Harris, 2001). Furthermore, the enrichment of high field-strength elements ((Ti, Zr, Hf, Nb, Ta, Mo, W) relative to UCC is related to clays and titanium-bearing minerals (Kiaeshkevarian et al., 2020). The depletion of Sr relative to UCC indicates plagioclase leached by weathering (Jasy et al., 2010).

The high Ga values (max. 285.2 ppm) in the gossan suggest that the gallium is incorporated in the structure of the kaolinite/fraipontite while Fe-(oxyhydr)oxides (goethite, hematite) tranported the Ga that was released from the hydrothermal ore (De Vos and Tarvainen, 2006; Santos et al., 2023).

The high Ba in the mineralised dolomitic limestone and limestone compared to non-mineralised limestone indicate that the Ba is associated with high Zn and Pb contents in the sulphide veins that depend on fault-fractured zones (Hosseini-Dinani and Aftabi, 2016).

The high REE values in the clays relative to UCC values, which has REE of 148.14 (Rudnick and Gao, 2000) indicates REE enriched within clay-sized particles (Wang et al., 2014). The enrichment of LREE relative to HREE in the dolomitic limestone and limestone and the REE values suggest the interaction of hydrothermal fluids with marine limestones similar to the values in the Riópar Zn-(Fe-Pb) deposit in Spain (Navarro-Ciurana et al., 2023). The high LREE/HREE, flat HREE patterns and negative Eu anomaly in the clays indicate sediments derived mainly from felsic rocks of the upper continental crust but with some contribution of a mafic component (Akarish and El-Gohary, 2011; Rahman et al., 2020). The negative Ce anomaly is consistent with the addition of REE straight from seawater or porewater in an oxic environment therefore this also indicates red clay (detrital) within marine sediments with the interaction of two different fluids (Nagarajan et al., 2011). Furthermore, Ce leached downwards in the lower section due to a low rate of oxidation (Keaherman et al., 2020). The positive Ce anomaly in the clays may reflect Ce^{+4} incorporation in Fe-(oxyhydr)oxide (Mondillo et al., 2019) reflecting acidic and oxidizing conditions in the upper section (Keaherman et al., 2020).

CONCLUSIONS

This study contributes to a characterization of residual and zinc clays in theTekneli and Delikkaya sulphide and non-sulphide Pb-Zn deposits and an analysis of the mechanisms of their formation. The MVT Tekneli and Delikkaya sulphide and non-sulphide Pb-Zn deposits are developed in carbonate platform sequences associated with faults and fractures and brecciated limestone/dolomitic limestones generally filled by galena and sphalerite in karstic caves formed in three successive stages in the study area. The Tekneli and Delikkaya non-sulphide mineral assemblage consists of smithsonite, goethite, hematite, rarely cerussite, and anglesite associated with residual and Zn clays.

The red residual clays (smectite, illite, rarely kaolinite) occur as stains and filling karstic cavities in the carbonate-hosted Tekneli and Delikkaya Pb-Zn deposits under supergene conditions. Zn clays (fraipontite, sauconite) are connected with how the Zn-rich meteoric water and residual clays interacted with karst growth in the Tekneli and Delikkaya Pb-Zn deposits. Mineralogical analyses (XRD, FTIR and SEM) showed that the Zn-rich clayey material consists of dominant fraipontite, rarely sauconite and occurred authigenically by the partial dissolution of detrital illite in the study area. Furthermore, the high zinc grade (max. 14.8%) in the zinc clays related to the sulphides may enable the discovery of high zinc potential.

The major element correlations, UCC values and slight enrichment of LREE relative to HREE with a negative Eu and negative /positive Ce anomalies in the clays suggest sediments derived from alteration of feldspar in mainly felsic rocks under oxic conditions during weathering. This study shows that Zn clays in karstic cavities might be of economic interest.

Acknowledgements. This present study was supported financially by the Scientific Research Projects Fund of Eskişehir Osmangazi University in the framework of Project 2020-3107, and consist of the second author's MSc study, supervised by the first author. This paper was presented at the 17th ICC2022, held in İstanbul, Turkey.

Authors contributions

Hülya Erkoyun: Field studies, Determination of the analyzed data, Drafting of the manuscript.

Ali Jawadi: Field studies, Determination of the analyzed data, Visualization.

Funding information

This present study was supported financially by the Scientific Research Projects Fund of Eskişehir Osmangazi University in the framework of Project 2020-3107.

Data Availability

All data are available in the two Tables and 11 Figures included here.

Code availability

Not applicable

Declarations

Conflicts of interest/Competing interests

The authors declare that there is no conflict of interest or competing interests.

Ethics approval and consents to participate

Not applicable

REFERENCES

Akarish, A.I.M., El-Gohary, A.M., 2011. Provenance and source area weathering derived from the geochemistry of Pre-Cenomanian sandstones, east Sinai, Egypt. Jornal of Applied Sciences, **11**: 3070–3088; https://scialert.net/abstract/?doi=jas.2011.3070.3088

Akinyemi, S.A., Adebayo, O.F., Ojo, O.A., Fadipe, O.A., Gitari, W.M., 2013. Mineralogy and geochemical appraisal of paleo-redox indicators in Maastrichtian outcrop shales of Mamu Formation, Anambra Basin, Nigeria. Journal Natural Sciences Research, **3:** 48–64.

Altuncu, S., 2000. Mineralogy and genesis of carbonate-bearing zinc-lead deposits of Meydan Yaylası-Karagöl-İspirtepe (Niğde) region (in Turkish with English summary). MSc. thesis, Niğde University, Niğde.

Arfè, G., Mondillo, N., Balassone, G., Boni, M., Cappelletti, P., Di Palma, T., 2017. Identification of Zn-bearing micas and clays from the Cristal and Mina Grande zinc deposits (Bongará Province, Amazonas Region, Northern Peru). Minerals, **7**, 214; https://doi.org/10.3390/min7110214

Ayhan, A., 1983. Aladağ (Yahyalı-Çamardı) yöresi karbonatlı çinko-kurşun yatakları (in Turkish). Türkiye Jeoloji Kurumu Bülteni, **26:** 107–116.

Balossone, G., Nietob, F., Arfèa, G., Bonia, M., Mondillo, N., 2017. Zn-clay minerals in the Skorpion Zn nonsulphide deposit (Namibia): identification and genegic clues revealed by HRTEM and AEM study. Applied Clay Science, **150:** 309–322; https://doi.org/10.1016/j.clay.2017.09.034

Bechtel, A., Savin, S.M., Hoernes, S., 1999. Oxygen and hydrogen isotopic compositon of clay minerals of the Bahloul Formation in the region of the Bou Grine-zinc-lead or deposit-Tunisia: evidence for fluid-rock interacton in the vicinity of salt dome cap rock. Chemical Geology, **156:** 191–207; https://doi.org/10.1016/s0009-2541(98)00185-5

Boni, M., 2003. Non-sulphide zinc deposits: a new (old) type of economic mineralization. SGA News, **15:** 6–13.

Boni, M., Large, D., 2003. Non-sulphide zinc mineralization in Europe: an overview. Economic Geology, **98:** 715–729; https://doi.org/10.2113/gsecongeo.98.4.715

Boni, M., Mondillo, N., 2015. The "Calamines" and the "Others": The great family of supergene nonsulphide zinc ores. Ore Geology Reviews, **67:** 208–233; https://doi.org/10.1016/j.oregeorev.2014.10.025

Boni, M., Balassone, G., Arseneau, V., Schmidt, P., 2009. The nonsulphide zinc deposit at Accha (southern Peru): geological and mineralogical characterization. Economic Geology, **104**: 267–289; https://doi.org/10.2113/gsecongeo.104.2.267

Boni, M., Terraciano, R., Balassone, G., Gleeson, S.A., Matthews, A., 2011. The carbonate hosted willemite prospects of the Zambezi Metamorphic Belt (Zambia). Mineralium Deposita, **46**: 707–729; https://doi.org/10.1007/s00126-011-0338-7

Brindley, G.W., 1980. Quatitative X-ray mineral analyses of clays. Mineralogical Society Monograph, **5**: 411–438.

Buatier, M., Choulet, F., Petit, S., Chassagnon, R., Vennemann, T., 2016. Nature and origin of natural Zn clay minerals from the Bou Arhous Zn ore deposit: evidence from electron microscopy (SEM-TEM) and stable isotope compositions (H and O). Applied Clay Sciences, **132:** 377–390; https://doi.org/10.1016/j.clay.2016.07.004

Calvo, M., Viñals, J., Triviño, A., 2007. Zálesiíte, felsobanyaite and fraipontite, in a conglomerate in Prullans, La Cerdanya, Catalonia (Spain). Mineral Up, **I**: 49–51.

Ceyhan, N., 2003. Lead isotope geochemistry of Pb-Zn deposits from eastern Taurides, Turkey (in Turkish with English summary). MSc. thesis, Middle East Technical University, Ankara, Turkey.

Chamley, H., 1989. Clay Sedimentology. Springer, Berlin, Heidelberg.

Choulet, F., Charles, N., Barbanson, L., Branquet, Y., Sizaret, S., Ennaciri, A., Badra, L., Chen, Y., 2014. Non-sulphide zinc deposits of the Moroccan High Atlas: multi-scale characterization and origin. Ore Geology Reviews, **56:** 115–140; https://doi.org/10.1016/j.oregeorev.2013.08.015

Choulet, F., Buatier, M., Barbonson, L., Guégan, R., Ennaciri, A., 2016. Zinc-rich clay in supergene non-sulphide zinc deposits. Mineralium Deposita, **51:** 467–490; https://doi.org/10.1007/s00126-015-0618-8

Chukhrov, F.V., 1956. Zinc clays from the Akdzhal deposits in Kazakhstan (in Russian). Kory Vyvetrivaniya, **2**: 107–123.

Churakov, S.V., Dähn, R., 2012. Zinc adsorption on clays inferred from atomistic simulations and EXAFS spectroscopy. Environmental Science and Technology, **46:** 5713–5719; https://doi.org/10.1021/es204423k

Coppola, V., Boni, M., Gilg, H., Balassone, G., Dejonghe, L., 2008. The "calamine" nonsulphide Zn-Pb deposits of Belgium: Petrographical, mineralogical and geochemical characterization. Ore Geology Reviews, **33:** 187–210; https://doi.org/10.1016/j.oregeorev.2006.03.005

Çelik, F., Demir, N., Gürbüz, A., Bingöl, E., 2007. Stratigraphic and tectonic characteristics of the Siyah Aladağ nappe (Aladağ mountains, Eastern Taurides) (in Turkish with English summary). Yerbilimleri, **28:** 113–126.

Çiftçi, E., Yavuz, B., Ataç, A., 2006. Orto Toroslar Pb-Zn damar hyataklarının kükgürt izotop karakteristikleri (in Turkish). TÜBİTAK Report No: 102Y130.

Çopuroğlu, İ., 1996. Yahyalı Kayseri-Demirkazık Niğde-Çamardı Yöresi Çinko-Kurşun Yataklarının Mineralojisi ve Jenezi (in Turkish). MTA Dergisi, **118:** 35–46.

Daliran, F., Borg, G., Armstrong, R., Vennemann, T., Walther, J., Woodhead, J.D.J., 2007. Nonsulphiphide Zinc Deposits. Iran. The Hypogene Emplacement and Supergene Modification History of the Angouran Zinc Deposit, NW-Iran. BGR Reihe Berichte zur Lagerstätten-und Rohstoffforschung. BGR, Hannover.

De Putter, Th., André, L., Bernard, A., Dupuis, Ch., Jedwab, J., Nicaise, D., Perruchot, A., 2002. Trace element (Th, U, Pb, REE) behaviour in a cryptokarstic halloysite and kaolinite deposit from Southern Belgium: importance of "accessory" mineral formation of radioactive pollutant trapping. Applied Geochemistry, **17:** 1313–1328; https://doi.org/10.1016/S0883-2927(02)00022-7

De Wos, W., Tarvainen, T., 2006. Geochemical Atlas of Europe. Part 2, Geochemisrty of Elements. Geological Survey of Finland, Otamedia Oy Espoo.

Demir, N., 1998. Relationship between the zinc-lead ore deposits and regional geologic evolution in the Niğde-Çamardı-Tekneli region (in Turkish with English summary). Ph.D. thesis, Çukurova Üniversitesi, Adana, Turkey.

Demir, N., Bingöl, E., 2000. Aladağlar bölgesi oksit-karbonat tip Zn-Pb yataklarının yapısal jeoloji ile ilişkileri (in Turkish). Cumhuriyetin 75 yıldönümü Yerbilimleri ve Madencilik Kongresi, Maden Tetkik ve Arama Genel Müdürlüğü, Ankara: 573–589.

Demirören, S.S., 2010. Lead isotope characteristics of Pb-Zn mineralizations occurring in the Bolkardağ-Aladağlar ore district (in Turkish with English summary). MSc. thesis, Niğde Üniversitesi, Niğde, Turkey.

Dilek, Y., Whitney, D.L., 2000. Cenozoic crustal evolution in central Anatolia: Extension, magmatism and landscape development. In: Proceedings of the 3 rd International Conference on the Geology of the Eastern Mediterranean, Nicosia, Cyprus: 183–192.

Dong, W., Tokunaga, T.K., James, A., Davis, J.A., Wan, J., 2012. Uranium (VI) adsorption and surface complexation modeling onto background sediments from the F-Area Savannah River Site. Environmental Science Technology, **46:** 1565–1571; https://doi.org/10.1021/es2036256

Dypvik, H., Harris, N.B., 2001. Geochemical facies analysis of fine grained siliciclastics using Th/U, Zr/Rb and (Zr+Rb)/Sr ratios. Chemical Geology, **181:** 131–146; https://doi.org/10.1016/S0009-2541(01)00278-9

Eren, R.H., Uz, B., Özpeker, I., Seymen, İ., 1993. Toroslar'da Tekneli (Çamardı-Niğde) yöresinin tektoniği ve Pb-Zn mineralizasyonu (in Turkish). Yerbilimleri, **22:** 45–60.

Erkoyun, H., Kadir, S., Külah, T., 2022. Genesis of smectites associated with a coal seams succession of in the Neogene Orhaneli and Keles coal deposits (Bursa), NW Turkey. Clays and Clay Minerals, **70:** 628–629; https://doi.org/10.1007/s42860-022-00209-1

Escalante, A., Dipple, G.M., Barker, S.L.L., Tosdal, R., 2010. Defining trace-element alteration halos to skarn deposits hosted in heterogeneous carbonate rocks: case study from the Cu-Zn Antamina skarn deposit, Peru. Journal of Geochemical Exploration, **105:** 117–136; https://doi.org/10.1016/j.gexplo.2010.04.011

Fransolet, A.M., Bourguignon, P., 1975. Données nouvelles sur la fraipontite de Moresnet (Belgique). Bulletin de la Société Française de Minéralogie, **98:** 235–244.

Garnit, H., Bouhlel, S., Kraemer, D., Ben Halima, K., Beaudoin, G., 2022. Characterization and genesis of supergene karstic vanadium ores in the Djebba Pb-Zn district (Triassic Diapirs zone, North Eastern Tunusia). Journal of African Earth Sciences, **196:** 1–21; https://doi.org/10.1016/j.jafrearsci.2022.104688

Hanilçi, N., 2003. Formation of the carbonate-hosted Pb-Zn deposits in Central and Eastern Taurus (in Turkish with English summary). Ph.D. thesis, Natural Science Institute, Istanbul University, Istanbul.

Hanilçi, N., Öztürk, H., 2005. Mississippi valley type Zn-Pb deposits in the Aladağlar – Zamantý (Eastern Taurus) region: Ayraklý and Denizovasý Zn-Pb deposits, Turkey (in Turkish with English summary). Ýstanbul Earth Sciences Review, **18** (2): 23–43.

Hanilçi, N., Öztürk, H., 2011. Geochemical-isotopic evolution of Pb-Zn deposits in the Central and Eatern Taurides, Turkey. International Geology Review, **53**: 1478–1507; https://doi.org/10.1080/00206811003680008

Hanilçi, N., Öztürk, H., Kasapçı, C., 2019. Carbonate-hosted Pb-Zn deposits of Turkey. In: Mineral Resources of Turkey, Modern Approaches in Solid Earth Sciences (eds. F. Pirajno, C. Dönmez and M.B. Şahin): 497–533. Springer Nature, Switzerland.

Helvacı, C., Oyman, T., Gündoğan, İ., Sözbilir, H., Parlak, O., Kadir, S., Güven, N., 2018. Mineralogy and genesis of the Ni-Co lateritic regolith deposit of the Çaldağ area (Manisa, western Anatolia), Turkey. Canadian Journal of Earth Sciences, **55:** 252–271; https://doi.org/10.1139/cjes-2017-0184

Hitzman, M.W., Reynolds, N.A., Sangster, D.F., Allen, C.R., Carman, C., 2003. Classification, genesis, and exploration guides for non-sulphide zinc deposits. Economic Geology, **98:** 685–714; https://doi.org/10.2113/gsecongeo.98.4.685

Hosseini-Dinani, H., Aftabi, A., 2016. Vertical lithogeochemical halos and zoning vectors at Goushfil Zn-Pb deposit, Irankuh district, southwestern Isfahan, Iran: implications for concealed ore exploration and genetic models. Ore Geology Reviews, **72:** 1004–1021; https://doi.org/10.1016/j.oregeorev.2015.09.023

Iacoviello, F., Martini, I., 2013. Clay minerals in cave sediments and terra rossa soils in the Montagnola Senese karst massif (Italy). Geological Quarterly, **57** (3): 527–536; https://doi.org/10.7306/gq.1111

Jasy, J.B., Rahman, M.J.J., Yeasmin, R., 2010. Sand petrology of the exposed bar deposits of the Brahmaputra-Jamuna River, Bangladesh: Implications for provenance. Bangladesh Geoscience Journal, **16:** 1– 22.

Jerzykowska, I., Majzlan, J., Michalik, M., Göttlicher, J., Steininger, R., Blachowski, A., Ruebenbauer, K., 2014. Mineralogy and speciation of Zn and As in Fe-oxide-clay aggregates in the mining waste at the MVT Zn-Pb deposits near Olkusz, Poland. Chemie der Erde, **74**: 393–406; https://doi.org/10.1016/j.chemer.2014.03.003

Jiang, Y., Qian, H., Zhou, G., 2016. Mineralogy and geochemistry of different morphological pyrite in late Permian coals, South China. Arabian Journal of Geosciences, **9:** 1–18; https://doi.org/10.1007/s12517-016-2612-6

Jönsson, J., Jönsson, J., Lövgren, L., 2006. Precipitation of secondary Fe (III) minerals from acid mine drainage. Applied Geochemistry, **21:** 437–445; https://doi.org/10.1016/j.apgeochem.2005.12.008

Kadir, S., Aydoğan, M., Elitok, Ö., Helvacı, C., 2015. Composition and genesis of the nickel-chrome-bearing nontroniteand montmorillonite in laterized ultramafic rocks in the Murat Dağı region (Uşak, Western Anatolia), Turkey. Clays and Clay Minerals, **63:** 163–184; https://doi.org/10.1346/CCMN.2015.0630302

Kahya, A., 2018. Geology and geochemistry of Madenköy (Ulukışla/Niğde) area carbonate-hosted Au-Ag-Zn±Pb deposits (in Turkish with English summary). Afyon Kocatepe University Journal of Science and Engineering, **18:** 648–663.

Kahya, A., Kuşcu, E., Yıldız, M., 2019. S and Pb isotope geochemistry of the carbonate-hosted Au-Ag-Zn±Pb deposits in the Maden village (Ulukışla-Niğde), Central Taurides, South Turkey. Neues Jahrbuch für Mineralogie Abhandlungen, **196**: 67–88; https://doi.org/10.1127/njma/2019/0166

Kärner, K., 2006. The metallogenesis of the Skorpion non-sulphide zinc deposit, Namibia. Dissertation, Universität Martin Luther.

Kiaeshkevarian, M., Calagaria, A.A., Abedinib, A., Shamanian, G., 2020. Geochemical and mineralogical features of karst bauxite deposits from the Alborz zone (Northern Iran): implications for conditions of formation, behavior of trace and rare earth elements and parental affinity. Ore Geology Reviews, **125:** 1–27; https://doi.org/10.1016/j.oregeorev.2020.103691

Kloprogge, J.T., Hammond, M., Hickey, L., Frost, R.L., 2001. A new low temperature synthesis route of fraipontite $(Zn, Al)_3$ $(Si, Al)_3$ $(OH)_4$. Materials Research Bulletin, **36:** 1091–1098; https://doi.org/10.1016/S0025-5408(01)00561-X

Kuşcu, M., Cengiz, O., 2001. Genesis of the Middle Taurus carbonate-hosted Zn-Pb deposits by stable isotope (S34/32) ratios (in Turkish with English summary). Türkiye Jeoloji Bülteni, **44:** 59–73.

Large, D., 2001. The geology of non-sulphide zinc deposits-an overview. Erzmetall, **54:** 264–276.

Liu, Y.C., Hou, Z.Q., Yang, Z.S., Tian, S., Yang, T.N, Song, Y.C., Zhang, H.R., Carranza, E.J.M., 2011. Formation of the Dongmozhazhua Pb-Zn deposit in the thrust-fold setting of the Tibetan Plateau, China: Evidence from fluid inclusion and stable isotope data. Resource Geology, **61:** 384–406; https://doi.org/10.1111/j.1751-3928.2011.00174.x

McGuire, M.K., 2012. Distribution of cogenetic iron and clay deposits in the central Appalachian region (in Turkish with English summary). MSc. thesis, Pittsburgh University.

Mengeloğlu, M.K., 1998. Doğu Akdeniz Bölgesi Kurşun–Çinko envanteri (in Turkish). Mineral Research and and Expoloration of Turkey (MTA) Report No. **11950:**1–79.

Merlino, S., Orlandi, P., 2001. Carraraite and zaccagnaite, two new minerals from the Carrara marble quarries: their chemical compositons, physical properties, and structural features. American Mineralogist, **86:** 1293–1301; https://doi.org/10.2138/am-2001-1017

Micheletti, F., Fornelli, A., Spalluto, L., Parise, M., Gallicchio, F.T., Festa, V., 2023. Petrographic and geochemical inferences for genesis of terra rossa: a case study from the Apulian Karst (Southern Italy). Minerals, **13**, 499; https://doi.org/10.3390/min13040499

Mondillo, N., Boni, M., Balassone, G., Villa, L.M., 2014. The Yanque prospect (Peru): from polymetallic Zn-Pb mineralization to a nonsulphide deposit. Economic Geology, **109:** 1735–1762; https://doi.org/10.2113/econgeo.109.6.1735

Mondillo, N., Nieto, F., Balassone, G., 2015. Micro and nano-characterization of Zn-clays in nonsulphide supergene ores of southern Peru. American Mineralogist, **100:** 2484–2496; https://doi.org/10.2138/am-2015-5273

Mondillo, N., Balassone, G., Boni, M., Chelle-Michou, C., Cretella, S., Mormone, A., Putzolu, F., Santoro, L., Scogniamiglio, G., Tarallo, M., 2019. Rare earth elements (REE) in A and Fe-(Oxy)-hydroxides in bauxites of Provence and Languedoc (Southern France): implications fort he potential recovery of REEs as by-products of bauxite mining. Minerals, **9,** 504; https://doi.org/10.3390/min9090504

Mongelli, G., 1997. Ce-anomalies in the textural components of Upper Cretaceous karst bauxites from the Apulian carbonate platform (southern Italy). Chemical Geology, **140**: 69–79; https://doi.org/10.1016/S0009-2541(97)00042-9

Moore, D.M., Reynolds, R.C., 1989. X-Ray Diffraction and the Identification and Analysis of Clay Minerals. Oxford University Press.

Navarro-Ciurana, D., Corral, I., Corbella, M., 2023. A tool for Zn-Pb MVT exploration by combining C and O isotopes and REE geochemistry of dolomite. Ore Geology Reviews, **156:** 1–24; https://doi.org/10.1016/j.oregeorev.2023.105405

Özbek, A.C., 2014. Alteration mineralogy and stable isotope characteristics of carbonate hosted Pb-Zn ore deposits in Central and Eastern Taurides (in Turkish with English summary). MSc. thesis, İstanbul Teknik University.

Öztürk, H., Hanilçi, N., 2009. Metallogenic evaluation of Turkey: implications fot tin sources of Bronze Age in Anatolia. TUBA-AR-Turkish Academy of Sciences Journal of Archaeology, **12:** 105–116; https://doi.org/10.4236/ad.2018.62004

Parsa, M,. Maghsoudi, A., 2018. Controls on Mississippi Valley-type Zn-Pb mineralization in Behabad district, Central İran: constraints from spatial and numerical analyses. Journal of African Earth Sciences, **140:** 189–198; https://doi.org/10.1016/j.jafrearsci.2018.01.012

Pekdemir, F., 2010. Investigation of mineralogycal properties and formation conditions of oxide zones observed in Pb-Zn deposits at Aladaglar (Delikkaya-Tekneli) (in Turkish with English summary). MSc. thesis, Niğde Üniversitesi, Niğde, Turkey.

Pfaff, K., Wagner, T., Markl, G., 2009. Fluid mixing recorded by mineral assemblege and mineral chemistry in a Mississippi Valley-type Pb-Zn-Ag deposit in Wiesloch, SW Germany. Journal of Geochemical Exploration, **101,** 81; https://doi.org/10.1016/j.gexplo.2008.12.022

Pirajno, F., Burlow, L., Huston, D., 2010. The Magellan Pb deposit, Western Australia: a new category within the class of supergene non-sulphide mineral systems. Ore Geology Reviews, **37:** 101–113; https://doi.org/10.1016/j.oregeorev.2010.01.001

Poot, J., Yans, J., Verhaert, M., Dekoninck, A., Maacha, L., Oummouch, A., El Basbas, A., 2020. Characterization of weathering processes of the Giant copper deposit of Tizert (Igherm Inlier, Anti-Atlas, Morocco). Minerals, **10**, 620; https://doi.org/10.3390/min10070620

Pour, A.B., Park, T.-Y.S, Park, Y., Hong, J.K., Zoheir, B., 2018. Application of multi-sensor satellite data for exploration of Zn-Pb sulphide mineralization in the Franklinin Basin, North Greenland. Remote Sensing, **10:** 1–36; https://doi.org/10.3390/rs10081186

Rahman, M.J.J., Suzuki, S., 2007. Geochemistry of sandstones from the Miocene Surma Group, Bengal Basin, Bangladesh: Implication for provenance, tectonic setting and weathering. Geochemical Journal, **41:** 415–428; https://doi.org/10.2343/geochemj.41.415

Rahman, Md A., Das, S.C., Pownceby, M.I., Tardio, J., Alam, Md S., Zaman, N., 2020. Geochemistry of recent Brahmaputra River sediments: Provenance, tectonics, source area weathering and depositional environment. Minerals, **10**, 813; https://doi.org/10.3390/min10090813

Reich, M., Vasconcelos, P.M., 2015. Geological and economic significance of supergene metal deposits. Elements, **11**: 305–310; https://doi.org/10.2113/gselements.11.5.305

Reynolds, N.A., Chisnall, T.W., Kaewsang, K., Keesaneyabutr, C., Taksavasu, T., 2003. The Padaeng supergene nonsulphide zinc deposit, Mae Sod, Thailand. Economic Geology, **98:** 773–785; https://doi.org/10.2113/gsecongeo.98.4.773

Ross, C.S., 1946. Sauconite - a clay mineral of the montmorillonite group. American Mineralogist, **31**: 411–424.

Rudnick, R.L., Gao, S., 2014. Composition of the Continental Crust. In: The Crust (eds. H.D. Holland and K.K. Turekian): 1–51. Treatise on Geochemistry, 2nd edn., Oxford, Elsevier.

Sangameshar, S.R., Barnes, H.L., 1983. Supergene processes in zinc-lead-silver sulphide ores in carbonates. Economic Geology, **78**: 1379–1397; https://doi.org/10.2113/gsecongeo.78.7.1379

Santos, P.H.C.d., Costa, M.L.d., Roerdink, D.L., 2023. Geochemical and isotopic fractionation in the hypogene ore, gossan, and saprolite of the Alvo 118 deposit: Implications for copper exploration in the regolith of the Carajás Mineral Provinve. Minerals, **13**, 1441; https://doi.org/10.3390/min13111441

Şahin, Z., 2005. Geology of the Çadırkaya (Yahyalı-Kayseri) lead-zinc deposits (in Turkish with English summary). MSc. thesis, Cumhuriyet Üniversitesi, Sivas, Turkey.

Taylor, S.R., McLennan, S.M., 1985. The Continental Crustal: Its Composition and Evolution. Blakwell, Oxford, UK.

Tekeli, O., 1980. Structural evolution of Aladağ Mountains in Taurus Belt (in Turkish with English summary). Türkiye Jeoloji Kurumu Bülteni, **23**: 11–14.

Tekeli, O., Aksay, A., Ürgün, B.M., Işık, A., 1983. Geology of Aladağ Mountains (in Turkish with English summary). In: Proceedings of the International Symposium on the Geology of the Taurus Belt (eds. O. Tekeli and M.C. Göncüoğlu): 143–158. General Directorate of Mineral Research and Exploration Ankara.

Tekin, E., 2009. Trace element geochemistry of the lead-zinc deposits in the Yahyalý (Kayseri) region (in Turkish with English summary). MSc thesis, Cumhuriyet Üniversitesi, Sivas, Turkey.

Temur, S., 1992. Geochemical investigation of the zinc-lead deposits in the Bolkardağız (Ululukışla Niğde-Turkey) district (in Turkish with English summary). Geological Bulletin of Turkey, **35:** 101–114.

Terracciano, R., 2008. Willemite mineralisation in Namibia and Zambia. Dissertation, Università degli Studi di Napoli Federico II.

Tümüklü, A., Altuncu, S., Özgür, F.Z., 2018. Evaluation of Nigde Massif in terms of ore deposits (in Turkish with English summary). Ömer Halisdemir University Journal of Engineering Sciences, **7**: 1119–1123; https://doi.org/10.28948/ngumuh.502294

Verhaert, M., Bernard, A., Dekoninck, A., Lafforgue, L., Saddiqi, O., Yans, J., 2017. Mineralogical and geochemical characterization of supergene Cu-Pb-Zn-V ores in the Oriental High Atlas, Morocco. Mineralium Deposita, **52**: 1049–1068; https://doi.org/10.1007/s00126-017-0753-5

Yalçın, M.G., Altuncu, S., 2004. Mineralogy and geochemical properties of İspirtepe (Niğde) carbonaceous's lead-zinc deposits (in Turkish with English summary). Pamukkale Üniversitesi Mühendislik Fakultesi Mühendislik Bilimleri Dergisi, **10**: 57–65.

Yıldırım, S., 2008. History of lead–zinc mining in the Anatolia (in Turkish with English summary). In: The geology, mining, and existing problems of Turkish Pb-Zn deposits (eds. H. Öztürk, N. Hanilçi, A. Kahriman and S. Özkan): 5–32. İstanbul University, İstanbul.

Wang, L., Liang, T., Zhang, Q., Li, K., 2014. Rare earth element components in atmospheric particulates in the Bayan Obo mine region. Environmental Researh, **131:** 64–70; https://doi.org/10.1016/j.envres.2014.02.006

Whitney, D.L., Evans, B.W., 2010. Abbreviations for names of rock-forming minerals. American Mineralogist, **95:** 185–187; https://doi.org/10.2138/am.2010.3371

Will, P., Friedrich, F., Hochleitner, R., Gilg, H.A., 2014. Fraipontite in the hydrothermally overprinted oxidation zone of the Preguiça mine, Southern Portugal. Mid-European Clay Conference, Dresden.

Wronkiewicz, D.J., Condie, K.C., 1987. Geochemistry of Archean shales from the Witwatersrand Supergroup South Africa: source-area weathering and provenance. Geochimica et Cosmochimica Acta, **51:** 2401–2416; https://doi.org/10.1016/0016-7037(87)90293-6

Wu, H., Jiang, Z., Huang, Q., Lan, F., Liao, H., Li, T., Huang, C., 2023. Geochemistry of weathering cover and the amin influencing factors in karst area of Guilin, southwest China. Water, **15,** 2944; https://doi.org/10.3390/w15162944

Zviagina, B.B., McCarty, D. K., Srodon, J., Victor, A.D., 2004. Interpretation of infared spectra of dioctahedral smectites in the region of OH-stretching vibrations. Clays and Clay Minerals, **52:** 399–410; https://doi.org/10.1346/CCMN.2004.0520401